J. Fluid Mech. (2005), *vol.* 535, *pp.* 111–142.
doi:10.1017/S0022112005004660 Printed in the United Kingdom

On near resonances and symmetry breaking in forced rotating flows at moderate Rossby number

By LESLIE M. SMITH[1] AND YOUNGSUK LEE[2]

[1]Departments of Mathematics and Engineering Physics, University of Wisconsin, Madison, WI 53706, USA

[2]Department of Mathematics, Simon Fraser University, Burnaby, BC V5A 1S6, Canada

(Received 14 September 2004 and in revised form 3 February 2005)

Numerical simulations are used to study a series of reduced models of homogeneous, rotating flow at moderate Rossby numbers $Ro \approx 0.1$, for which both numerical and physical experiments show the generation of quasi-two-dimensional vortices and symmetry breaking in favour of cyclones. A random force at intermediate scales injects energy at a constant average rate. The nonlinear term of reduced models is restricted to include only a subset of triad interactions in Fourier space. Reduced models of near-resonant, non-resonant and near two-dimensional triad interactions are considered. Only the model of near resonances reproduces all of the important characteristics of the full simulations: (i) efficient energy transfer from three-dimensional forced modes to two-dimensional large-scale modes, (ii) large-scale energy spectra scaling approximately as k_h^{-3}, where k_h is the wavenumber in the plane perpendicular to the axis of rotation, and (iii) strong cyclone/anticyclone asymmetry in favour of cyclones. Non-resonances, defined as the complement to near resonances, act to reduce the energy transfer to large scales.

1. Introduction

There has been a series of numerical investigations of anisotropic wave-turbulence dynamics in dispersive-wave models of geophysical flows, forced at intermediate scales. Interest has focused on energy accumulation in the large-scale zero-frequency modes and the corresponding generation of anisotropic coherent structures, such as large-scale zonal flows and vortices. Identifying the mechanisms for the formation of such structures in idealized simulations may help in understanding their formation in planetary flows. Chekhlov *et al.* (1996), followed by Smith & Waleffe (1999), Marcus, Kundu & Lee (2000), Huang, Galperin & Sukoriansky (2001), Manfroi & Young (2002) and Smith (2004), observed the generation of zonal flows on the two-dimensional β-plane. In homogeneous rotating and stratified flow governed by the three-dimensional Boussinesq equations, Smith & Waleffe (2002) observed different large-scale structures, ranging from horizontal shear layers to vortical columns, depending on the ratio N/f, where N is the buoyancy frequency and f is the Coriolis parameter (twice the frame rotation rate).

For purely rotating flows, energy input by intermediate-scale forcing has been observed to self-organize into large-scale columnar vortices aligned with the rotation axis. Following convention, the axis of rotation is taken to be $\hat{\mathbf{z}}$, and k_z ($k_h = (k_x^2 + k_y^2)^{1/2}$)

is the component of the wavevector parallel (perpendicular) to the rotation axis. The two-dimensional plane is the horizontal plane with $k_z = 0$. In homogeneous flows, Hossain (1994), Smith & Waleffe (1999) and Chen *et al.* (2004) observed significant transfer of energy from the forced, three-dimensional intermediate scales to two-dimensional large scales. For flow in a periodic cube with resolution 128^3 Fourier modes, Smith & Waleffe (1999) noted a symmetry breaking in favour of large-scale cyclonic vortical columns for moderate Rossby numbers below an $O(1)$ critical value. In that study, the Rossby number was based on the rate of energy input and the peak wavenumber of the force, which was white in time with Gaussian spatial correlation function. Lollini & Godeferd (1999) studied the emergence of vortical columns in inhomogeneous rotating flows, with confinement in the direction of the rotation axis and forcing localized in physical space. They found that cyclones dominated anticyclones for high Reynolds numbers and moderate local Rossby numbers $Ro_l \approx 0.2$–0.3, based on a local velocity and length scale away from the forcing. The latter numerical experiments were designed to mimic the laboratory experiments by Hopfinger, Browand & Gagne (1982), who used an oscillating grid to produce turbulence in a rotating tank. With grid Rossby numbers in the range $Ro_g \approx 3$–33, defined as the ratio of grid to Coriolis frequencies, Hopfinger *et al.* (1982) noted the dominance of cyclonic vortices for the smaller grid Rossby numbers; the local Rossby number away from the grid was $Ro_l \approx 0.05$. Baroud *et al.* (2003) studied flow in a rotating annulus with forcing created by pumping water into (out of) the annulus through an inner (outer) ring of holes on the bottom of the channel. At $Ro \approx 0.1$, this set-up leads to a nearly two-dimensional flow in which vortices are advected by a counter-rotating azimuthal jet. Their Rossby number was defined as the ratio of the root-mean-square vorticity to the Coriolis frequency. Baroud *et al.* (2003) observed that cyclones were more likely to preserve their shape and to be carried azimuthally by the jet without losing their coherence. Well-defined vortices were also observed in laboratory experiments by Longhetto *et al.* (2002) using the 'Coriolis' rotating tank in Grenoble. Turbulence was initially generated by horizontal motion of a rake, and then allowed to develop freely. Cyclones were in general much stronger and lived longer than anticyclones for values of the initial Rossby number of approximately one, based on the speed and teeth spacing of the rake.

Our focus is on the role of near-resonant triad interactions in three-dimensional rotating flow forced at intermediate scales. We consider moderate Rossby numbers $Ro \approx 0.1$, for which cyclone dominance appears to be well-established by both numerical and laboratory experiments with forcing (despite different definitions for the Rossby number). Nonlinear two-dimensionalization, the emergence of vortices and cyclone/anti-cyclone asymmetry have also been observed in physical and numerical experiments of decaying rotating turbulence. The literature on rotating decay has provided important insights into the development of anisotropy in rotating flows in general, and is discussed in § 2.

For simplicity we consider homogeneous flow in a periodic cube, with constant background rotation rate. We ask if a reduced model including only interactions between near resonances can reproduce three important features observed at $Ro \approx 0.1$ in simulations including all triad interactions: (i) significant energy transfer from forced three-dimensional intermediate scales to two-dimensional large scales; (ii) scaling of the large-scale energy spectra approximately $E(k) \approx E(k_h; k_z = 0) \propto k_h^{-3}$, and (iii) dominance of cyclonic vortical columns (Hossain 1994; Smith & Waleffe 1999). Near-resonant triads satisfy $\sigma_s(\boldsymbol{k}) + \sigma_s(\boldsymbol{p}) + \sigma_s(\boldsymbol{q}) = O(Ro)$, where $\sigma_s(\boldsymbol{k}) = sk_z/k_h$ for $s = \pm 1$ are the wave frequencies of the two linear eigenmodes with wavevector $\boldsymbol{k}$, and the

velocity field is represented as a superposition of inertial waves (the linear eigenmodes). Using multiple-scales analysis, Newell (1969) showed that near resonances, in addition to exact resonances with $\sigma_s(\boldsymbol{k})+\sigma_s(\boldsymbol{p})+\sigma_s(\boldsymbol{q})=0$, are important on a time scale of $O(1/Ro)$, where the linear time scale is $O(Ro)$.

It has been recognized for many years that the nonlinear two-dimensionalization observed in both forced and decaying, rotating turbulence does not follow directly from the Taylor–Proudman theorem for inviscid slowly varying flow in the linear limit. Furthermore, since the Taylor–Proudman theorem says nothing about the energy level in the component of velocity parallel to the rotation axis as compared to the energy level in the perpendicular velocities, the theorem does not predict the observed tendency toward two-dimensional and *two-component* flow, with much lower levels of energy in the parallel velocity component (e.g. Cambon, Mansour & Godeferd 1997; Smith & Waleffe 1999). Recently, Constantin (2004) obtained a bound on the parallel gradients of the Lagrangian displacement that vanishes linearly with the local Rossby number.

Chen *et al.* (2004) performed periodic cube simulations with the same resolution (128^3 modes) as Smith & Waleffe (1999), but with significantly smaller Rossby numbers (as small as $Ro=(\varepsilon_f k_f^2)^{1/3}/f\approx 10^{-3}$, where ε_f and k_f are, respectively, the energy input rate and the peak wavenumber of the force). Their purpose was to demonstrate numerically the decoupling between three-dimensional modes and two-dimensional modes with $k_z=0$, at first order in a Rossby number expansion. First-order decoupling was shown for a general bounded domain by Greenspan (1969), and for periodic domains by Waleffe (1993), Embid & Majda (1996) and Babin, Mahalov & Nicolaenko (1996, 2000). In a wave decomposition, first-order interactions are between exactly resonant triads satisfying $\sigma_s(\boldsymbol{k})+\sigma_s(\boldsymbol{q})+\sigma_s(\boldsymbol{q})=0$. The two-dimensional modes with $k_z=0$ form a slow manifold and interactions between them are trivially resonant. First-order decoupling between two-dimensional and three-dimensional modes means that resonant interactions between two inertial waves and one two-dimensional mode cannot transfer energy directly to the two-dimensional mode. With forcing at intermediate scales, and for $Ro\approx 10^{-3}$, Chen *et al.* (2004) observed an inverse cascade among two-dimensional modes only, with large-scale energy spectrum $E(k_h)\propto k_h^{-5/3}$ and no asymmetry (see also Kraichnan 1967; Smith & Yakhot 1994). We conjecture that the resolution of 128^3 Fourier modes is not sufficient to resolve the near-resonant interactions with $\sigma_s(\boldsymbol{k})+\sigma_s(\boldsymbol{p})+\sigma_s(\boldsymbol{q})=O(10^{-3})$ that would lead to non-trivial coupling for nonlinear time scales, in this case on the order of one thousand times longer than the linear time scale.

First-order decoupling between the slow manifold and fast waves is an important feature of many dispersive-wave models for geophysical flows, and in particular for β-plane flow (Longuet-Higgins & Gill 1967), for three-dimensional rotating, stratified flow (Bartello 1995; Embid & Majda 1998; Majda & Embid 1998) and for purely stratified flow (Phillips 1968; Lelong & Riley 1991). However, near-resonant triads play a role for moderate Rossby numbers $Ro\approx 0.1$, in addition to exact resonances (see e.g. Newell 1969). They are likely also to play a role for any small finite Rossby number on long time scales in sufficiently large domains (see the discussion in the next paragraph). Finally, since two-dimensional interactions are not affected by rotation, the symmetry breaking between cyclones and anticyclones that has been observed in numerical and laboratory experiments must originate from near-resonant triads and/or other higher-order effects (e.g. resonant quartets). Our numerical simulations at moderate Rossby numbers indicate that near resonances are responsible for increased energy transfer to large scales resulting in steeper large-scale

energy spectra $E(k) \approx E(k_h, k_z = 0) \propto k_h^{-3}$, as well as strong asymmetry in favour of cyclones.

When discussing the slow manifold and first-order decoupling/higher-order coupling, one must take care to distinguish between the discrete wavenumbers in periodic domains and continuous wavenumbers in an infinite domain. Indeed, both periodic domains and infinite domains are idealizations. Neither reflects the complete dynamics of physical flows in bounded domains, with other complexities such as boundary-layer eruptions and energy transfer by wave reflections (Greenspan 1990). In an unbounded domain, exact resonances are always present, but comprise a set of measure zero. For continuous wavenumbers, Cambon, Rubinstein & Godeferd (2004) have shown that first-order decoupling is invalid for $k_z \to 0$, since coupling terms arise from principal-value integrals corresponding to off-resonant interactions. In periodic domains, wavenumbers are discrete and the existence and number of exact resonances depends on domain size and aspect ratio. Purely two-dimensional interactions can be enhanced in relatively low resolutions where they receive a significant fraction of the energy input, and where exact/near resonances are becoming negligible for sufficiently small Ro. Simulations at finite resolution and finite times cannot necessarily capture the long-time dynamics implied by statistical closure theories or higher-order multiple-scales analyses. Differences between discrete and continuous wavenumbers have also been discussed in the context of other wave-turbulence systems. In studies of capillary waves, Pushkarev & Zakharov (2000) and Connaughton, Nazarenko & Pushkarev (2001) showed that for very low levels of nonlinearity, the number of near resonances captured by integer-valued wavevectors in a periodic box is insufficient to reflect the structure of the resonant manifolds, and that the effects of discreteness begin to play a role. In the numerical experiments by Pushkarev & Zakharov (2000), these discreteness effects lead to deviations from weak turbulence predictions, and in the extreme, they halt the nonlinear transfer of energy altogether. In our simulations of rotating flow at moderate Rossby number $Ro \approx 0.1$, the nonlinearity is large enough so that near resonances are adequately captured by the computational grid, and the time scale for coupling between three-dimensional fast waves and two-dimensional slow modes is not prohibitively long. With our non-dimensionalization based on the dimensional time scale L/U, the linear time scale is $O(Ro)$, the nonlinear time scale for exact resonances is $O(1)$, and the time scale for near resonances is $O(1/Ro)$ (see Newell 1969 and § 3).

The fluid dynamics governed by the Navier–Stokes equations in a rotating frame is of fundamental interest, but also has connection to geophysical applications. A predominance of cyclones is observed in mid-latitude atmospheric and oceanic flows. Pedlosky (1986, Chapter 1) estimates Rossby numbers $Ro \approx 0.1$ for flows in the Gulf Stream and for synoptic-scale flows at mid-latitudes. For example, typical mid-latitude synoptic-scale velocities U and length scales L are, respectively, $U \approx 20\,\mathrm{m\,s^{-1}}$ and $L \approx 1000\,\mathrm{km}$. Then the rotation rate $\Omega = 7.3 \times 10^{-5}\,\mathrm{s^{-1}}$ gives $Ro = U/(2\Omega L) \approx 0.14$. In many atmospheric and oceanic flows, both rotation and stratification are important. Although it is well-known that the quasi-geostrophic (QG) approximation for rotating and stratified flow does not exhibit asymmetry (see e.g. McWilliams 1990; McWilliams, Weiss & Yavneh 1999), next-order corrections to quasi-geostrophy lead to symmetry breaking in favour of cyclones (Hakim, Snyder & Muraki 2002; Muraki, Snyder & Rotunno 1999). The QG model and corrections to QG are simplifications of the Boussinesq equations assuming large horizontal length scales and the hydrostatic balance (Pedlosky 1986; Salmon 1998). On the other hand, numerical decay from balanced initial conditions of the rotating shallow-water equations leads

to a predominance of anticyclones as the initial Froude number is increased, where the Froude number is the ratio of characteristic fluid and gravitational speeds (Polvani *et al.* 1994). The latter result holds for Froude numbers Fr in the range $0.04 \leqslant Fr \leqslant 0.30$ and over a wide range of initial Rossby numbers $0.01 \leqslant Ro \leqslant 20$. Symmetry breaking has also been observed in the non-hydrostatic approximate equations derived by Julien, Knobloch & Werne (1998), valid for rapid rotation and small $|k_z|/k_h$. There is not necessarily a direct connection between the length and time scales associated with geophysical models and those of fundamental turbulence studies such as the present numerical investigation. However, it is likely that mechanisms for energy transfer and symmetry breaking in idealized simulations may also play a role in the dynamics of geophysical flows. For example, in the context of the nonlinear Schrödinger equation (which admits four-wave resonances), resonance broadening has been linked to the occurrence of freak waves in the ocean (Janssen 2002). Understanding the mechanisms for cyclone/anticyclone asymmetry and wave-mean flow interactions in rotating turbulence may help toward understanding similar observed phenomena in geophysical flows.

The remainder of the paper is organized as follows. The literature on rotating decay and statistical closure theories is reviewed in § 2, since this literature provides understanding of anisotropy development in rotating flows in general. In § 3, properties of the basic equations are reviewed, and the concept of a reduced model is introduced. Section 4 explains how we numerically calculate the nonlinear interactions for reduced models, when the quadratic nonlinearity can no longer be computed in physical space using fast Fourier transforms. The simulation results for three-dimensional rotating flow are presented in § 5, including reduced models for near resonances, non-resonances, and near-two-dimensional interactions. A summary and discussion are given in § 6.

2. Development of anisotropy in decaying rotating flows

The development of anisotropy in rotating flows has been studied most extensively for decaying rotating turbulence. The understanding developed in this literature is important background for all work on rotating flows, and is thus discussed below.

Pioneering experimental studies were conducted by Wigeland & Nagib (1978) and Jacquin *et al.* (1990). In both sets of experiments, turbulence in solid body rotation was generated by a flow of air passing through a rotating honeycomb and a turbulence-producing grid. Compared to isotropic decay, they observed an increase in the integral length scales involving velocity components perpendicular to the rotation axis. In contrast to the integral length scales, the Reynolds stress tensor remained nearly isotropic in both experiments. The Reynolds stress tensor, however, can be an ambiguous indicator of anisotropy as the flow develops toward a quasi-two-dimensional state, although strict two-dimensionality is not achieved. Isotropic three-dimensional three-component flow has $\langle u^2 \rangle = \langle v^2 \rangle = \langle w^2 \rangle$, where the velocity is $\boldsymbol{u} = u(\boldsymbol{x})\hat{\boldsymbol{x}} + v(\boldsymbol{x})\hat{\boldsymbol{y}} + w(\boldsymbol{x})\hat{\boldsymbol{z}}$ and $\langle\rangle$ indicates an ensemble average. For a general, statistically axisymmetric two-dimensional three-component incompressible flow, the velocity satisfies $\langle u^2 \rangle = \langle v^2 \rangle = \langle w^2 \rangle/2$, with $\boldsymbol{u} = u(x, y)\hat{\boldsymbol{x}} + v(x, y)\hat{\boldsymbol{y}} + w(x, y)\hat{\boldsymbol{z}}$. The velocity component w in two-dimensional three-component flow is effectively a passive scalar. Mixing of w in two-dimensional three-component flow would then lead, presumably, to two-dimensional two-component flow, with $\langle u^2 \rangle = \langle v^2 \rangle$ and $\langle w^2 \rangle = 0$. Thus, during decay from three-dimensional three-component initial conditions, the quantity $A = \langle w^2 \rangle / (\langle u^2 \rangle + \langle v^2 \rangle)$ grows initially from one-half (isotropy) as the flow

tends toward an axisymmetric state (Cambon *et al.* 1997; Morinishi, Nakabayashi & Ren 2001). The value one for two-dimensional three-component flow is not reached, however, perhaps because partial mixing of w drives the value of A back down ($A=0$ for two-dimensional two-component flow). These two competing tendencies obscure the effects of rotation if $\langle w^2\rangle/(\langle u^2\rangle+\langle v^2\rangle)$ and/or similar quantities are used to monitor the flow (Cambon *et al.* 1997, F. Waleffe, private communication).

Following Wigeland & Nagib (1978) and Jacquin *et al.* (1990) came a series of numerical experiments on rotating decay, using pseudo-spectral methods in a periodic domain (Bardina, Ferziger & Rogallo 1985; Bartello, Metais & Lesieur 1994; Cambon, Mansour & Squires 1994; Cambon *et al.* 1997). Consistent with the experiments, the direct numerical simulations (DNS) with 64^3 Fourier modes by Bardina *et al.* (1985) and Bartello *et al.* (1994) showed only a tendency toward two-dimensional flow by an increase in the appropriate integral length scales. However, the large-eddy simulations (LES) and hyperviscosity runs by Bartello *et al.* (1994) clearly showed the emergence of two-dimensional cyclonic vortices (and few or no anticyclonic vortices). The hyperviscosity runs suggested a range of Rossby numbers $0.1<Ro<0.4$ where three-dimensional modes most efficiently transfer energy to two-dimensional modes in the form of cyclonic vortices. Their Rossby number was defined by the initial velocity field as the ratio of root-mean-square vorticity in the $\hat{\boldsymbol{z}}$-direction to the Coriolis frequency.

Cambon *et al.* (1994) conducted a series of LES at higher resolution $128\times128\times512$, aimed at simulating growth of the integral length scales in an infinite domain, and demonstrated the existence of two transitions in the development of anisotropy. They defined a macro-Rossby number based on the root-mean-square velocity and an integral length scale. In addition, they defined the micro-Rossby number as the ratio of the root-mean-square vorticity and the Coriolis frequency. Anisotropy of the length scales was triggered when the macro-Rossby number was decreased to about unity; maximum anisotropy of the length scales and Reynolds stresses was achieved for macro-Rossby number smaller than unity but micro-Rossby number somewhat larger than unity (see also Cambon *et al.* 1997; Canuto & Dubovikov 1997; Morinishi *et al.* 2001).

Cambon *et al.* (1997) discussed how anisotropy can be fully captured in statistical theory. Representing the velocity field as a superposition of inertial waves with amplitudes $b_s(\boldsymbol{k})$ (see (3.7)), the ensemble-averaged energy and helicity are, respectively, $e(k_h,k_z)=(\langle b_+^*b_+\rangle+\langle b_-^*b_-\rangle)/2$ and $h(k_h,k_z)=k(\langle b_+^*b_+\rangle-\langle b_-^*b_-\rangle)/2$, where $s=\pm$, $*$ denotes the complex conjugate and brackets $\langle\rangle$ indicate an ensemble average. Although it is common to develop statistical theory based on energy and helicity, there is an additional second-order correlation $Z=\langle b_+^*b_-\rangle$. The quantity Z is zero in three-dimensional three-component isotropic flow, whereas $Z=-e$ in two-dimensional two-component flow, and in general Z provides critical information about the polarization (a reduction in the number of components) of the flow. In fact, a full description of the Reynolds stress requires all three quantities e, h and Z. Cambon *et al.* (1997) developed a model for rotating turbulence by EDQNM-type closure of the exact equations for energy e, helicity h and polarization Z (see also Cambon & Jacquin 1989; Jacquin *et al.* 1990). The EDQNM-type closure is based on helical modes, and is consistent with classical wave-turbulence theory if both the Rossby number and the heuristic damping effects vanish. New simulations of the closure equations suggest that the cyclone/anticyclone asymmetry is not outside the scope of statistical closure methods at finite Rossby number (C. Cambon, private communication).

Both weakly nonlinear theory and statistical theory of wave-turbulence systems are based on resonant interactions. Some of the original multiple-scales analyses are given by Benney & Saffman (1966) and Newell (1969). The Hamiltonian formulation of weak turbulence is described in Zakharov, Lvov & Falkovich (1992); in the limit $Ro \to 0$, the effects of exact resonances are retained in the equation for the ensemble-averaged second-order moments, which are closed using a random phase approximation. Galtier (2003) applied the Kuznetsov–Zakharov conformal transformation to the wave-kinetic equations for the case of nearly horizontal wavenumbers with $|k_z|/k_h \ll 1$, and thereby derived the angle-dependent anisotropic energy spectrum $e(k_h, k_z) \propto k_h^{-7/2}|k_z|^{-1/2}$ (Galtier 2003 works with $2\pi k_h e(k_h, k_z) \propto k_h^{-5/2}|k_z|^{-1/2}$). The total energy E is given by $E = 2\pi \int_{-\infty}^{\infty} \mathrm{d}k_z \int_0^{\infty} k_h e(k_h, k_z)\, \mathrm{d}k_h$ for axisymmetric flow, and the spectrum $e(k_h, k_z) \propto k_h^{-7/2}|k_z|^{-1/2}$ is consistent with forward transfer of energy from large to small scales. With an infrared cutoff k_o in the $\hat{\boldsymbol{z}}$-direction, Cambon *et al.* (2004) showed that the weak-turbulence theory for $|k_z|/k_h \ll 1$ predicts $e(k_h, k_z) \propto k_o^{-1/2}|k_z|^{-1/2}k_h^{-3}$. They developed a closure for $|k_z|/k_h \ll 1$, including the effects of the polarization $Z = \langle b_+^* b_- \rangle$. High-resolution 300^3 decay simulations of the closure equations support the anisotropic scaling $e(k_h, k_z) \propto k_o^{-1/2}|k_z|^{-1/2}k_h^{-3}$, and also suggest scaling for the spherically averaged spectrum $E(k) \propto k^{-3}$ (see also Bellet *et al.* 2004). Notice, however, that the scaling $E(k) \propto k^{-3}$ does not reflect a forward enstrophy cascade of flow confined to the two-dimensional horizontal plane.

3. Three-dimensional flow in a rotating frame

3.1. *The governing equations and properties*

A non-dimensional form of the Navier–Stokes equations for incompressible flow in a rotating frame is

$$\left.\begin{aligned} &\frac{\partial}{\partial t}\boldsymbol{u} + \frac{1}{Ro}\hat{\boldsymbol{z}} \times \boldsymbol{u} + (\boldsymbol{\nabla} \times \boldsymbol{u}) \times \boldsymbol{u} = -\boldsymbol{\nabla} P + \frac{1}{Re}\nabla^2 \boldsymbol{u} + \boldsymbol{f}, \\ &\boldsymbol{\nabla} \cdot \boldsymbol{u} = 0, \end{aligned}\right\} \tag{3.1}$$

where P is a pressure and $\boldsymbol{f}$ is an external force. The Rossby number Ro and the Reynolds number Re are given by

$$Ro = \frac{U}{2\Omega L} \quad \text{and} \quad Re = \frac{UL}{\nu}, \tag{3.2}$$

where Ω is the frame rotation rate, and L and U are characteristic length and velocity scales, respectively.

In the absence of external forcing, the inviscid linear limit of these equations admits wave solutions (Greenspan 1968) called inertial waves, of the form

$$\boldsymbol{u}(\boldsymbol{x}, t; \boldsymbol{k}, s) = \boldsymbol{h}_s(\boldsymbol{k}) \exp\left[\mathrm{i}\left(\boldsymbol{k} \cdot \boldsymbol{x} - \sigma_s(\boldsymbol{k})\frac{t}{Ro}\right)\right] + \text{c.c.}, \tag{3.3}$$

where c.c. denotes the complex conjugate, $\boldsymbol{k} = (k_x, k_y, k_z)$ is a three-dimensional wavevector and $s = \pm 1$ is the helicity. The eigenmodes $\boldsymbol{h}_s(\boldsymbol{k})$ are called helical modes and are given by

$$\boldsymbol{h}_s(\boldsymbol{k}) = \frac{1}{\sqrt{2}}(\hat{\boldsymbol{k}} \times \hat{\boldsymbol{\phi}} + \mathrm{i}s\hat{\boldsymbol{\phi}}), \tag{3.4}$$

with $\mathrm{i}^2=-1$, $\hat{\boldsymbol{k}}=\boldsymbol{k}/|\boldsymbol{k}|$, and $\hat{\boldsymbol{\phi}}=(\boldsymbol{k}\times\hat{\boldsymbol{z}})/|\boldsymbol{k}\times\hat{\boldsymbol{z}}|$. The dispersion relation for the wave frequency is

$$\sigma_s(\boldsymbol{k})=s\frac{k_z}{k}, \tag{3.5}$$

where $k=|\boldsymbol{k}|$. The relation (3.5) is homogeneous with respect to $\boldsymbol{k}$ since $\sigma(a\boldsymbol{k})=\sigma(\boldsymbol{k})$ for any scalar $a\neq 0$. For $\boldsymbol{k}=(0,0,k_z)$, expression (3.4) is singular and one may choose the following modes:

$$\boldsymbol{h}_s((0,0,k_z))=\tfrac{1}{2}(1+\mathrm{i}\,s\,\mathrm{sgn}(k_z),\,1-\mathrm{i}\,s\,\mathrm{sgn}(k_z),\,0), \tag{3.6}$$

where sgn is the sign function. The eigenmodes $\boldsymbol{h}_s(\boldsymbol{k})$ satisfy (i) that $\boldsymbol{k}$, $\boldsymbol{h}_1$, $\boldsymbol{h}_{-1}$ form an orthonormal basis, (ii) $\boldsymbol{h}_s(\boldsymbol{k})=\boldsymbol{h}^*_{-s}(\boldsymbol{k})$, (iii) $\boldsymbol{h}_s(-\boldsymbol{k})=\boldsymbol{h}^*_s(\boldsymbol{k})$ and (iv) $\mathrm{i}\boldsymbol{k}\times\boldsymbol{h}_s(\boldsymbol{k})=-sk\boldsymbol{h}_s(\boldsymbol{k})$ (i.e. $\boldsymbol{h}_s(\boldsymbol{k})$ is helical) (see Cambon & Jacquin 1989; Waleffe 1992, 1993; Constantin & Majda 1988).

One may represent $\boldsymbol{u}$ as a sum of inertial waves with amplitudes $b_s(t;\boldsymbol{k})$,

$$\boldsymbol{u}(\boldsymbol{x},t)=\sum_{\boldsymbol{k}}\sum_{s=\pm1} b_s(t;\boldsymbol{k})\boldsymbol{h}_s(\boldsymbol{k})\exp\left[\mathrm{i}\left(\boldsymbol{k}\cdot\boldsymbol{x}-\sigma_s(\boldsymbol{k})\frac{t}{Ro}\right)\right], \tag{3.7}$$

where $b_s(t;\boldsymbol{k})=b^*_s(t;-\boldsymbol{k})$ for reality. Then, the Navier–Stokes equations (3.1) yield

$$\left(\frac{\partial}{\partial t}+\frac{k^2}{Re}\right)b_{s_k}(\boldsymbol{k})=\sum_{\triangle_{kpq}}\sum_{s_p,s_q}C^{s_k s_p s_q}_{\boldsymbol{kpq}}b^*_{s_p}(\boldsymbol{p})b^*_{s_q}(\boldsymbol{q})\exp\left[\mathrm{i}\left(\sigma_{s_k}+\sigma_{s_p}+\sigma_{s_q}\right)\frac{t}{Ro}\right]. \tag{3.8}$$

Here $b_{s_k}(\boldsymbol{k})$ and σ_{s_k} are shorthand notations for $b_{s_k}(t;\boldsymbol{k})$ and $\sigma_{s_k}(\boldsymbol{k})$ respectively, and the first sum is over all triads $\triangle_{kpq}$ with $\boldsymbol{k}+\boldsymbol{p}+\boldsymbol{q}=\boldsymbol{0}$.† The effect of rotation now appears in the exponent of the integrating factor in (3.8). The coefficients $C^{s_k s_p s_q}_{\boldsymbol{kpq}}$ are given by

$$C^{s_k s_p s_q}_{\boldsymbol{kpq}}=(s_p p-s_q q)\left(\boldsymbol{h}^*_{s_p}\times\boldsymbol{h}^*_{s_q}\right)\cdot\boldsymbol{h}^*_{s_k} \tag{3.9}$$

and they satisfy

$$\left.\begin{aligned} &C^{s_k s_p s_q}_{\boldsymbol{kpq}}+C^{s_p s_q s_k}_{\boldsymbol{pqk}}+C^{s_q s_k s_p}_{\boldsymbol{qkp}}=0,\\ &s_k kC^{s_k s_p s_q}_{\boldsymbol{kpq}}+s_p pC^{s_p s_q s_k}_{\boldsymbol{pqk}}+s_q qC^{s_q s_k s_p}_{\boldsymbol{qkp}}=0 \end{aligned}\right\} \tag{3.10a}$$

and

$$C^{s_k s_p s_q}_{\boldsymbol{kpq}}=\left[C^{s_k s_p s_q}_{-\boldsymbol{k},-\boldsymbol{p},-\boldsymbol{q}}\right]^*,\quad \left[C^{s_k s_p s_q}_{\boldsymbol{kpq}}\right]^*=-C^{-s_k,-s_p,-s_q}_{\boldsymbol{kpq}}. \tag{3.10b}$$

The two equations in (3.10*a*), respectively, express energy and helicity conservation by triad interactions. The first equation in (3.10*b*) is a reality condition, and the second shows that the conjugate of the interaction coefficient is the negative of the interaction coefficient with the opposite helicities. Note that, for a given triad $(\boldsymbol{k},\boldsymbol{p},\boldsymbol{q})$, there are eight different interactions $(s_k s_p s_q)=(+,+,+),(+,+,-),\cdots,(-,-,-)$ depending on the helicities of the modes. We use properties (3.10*b*) in the direct computation of the nonlinear interactions in wavevector space, in order to simulate the dynamics of reduced models based on subsets of triad interactions (see § 4).

† One may use $\sum_{\boldsymbol{p}}$ with $\boldsymbol{q}=-\boldsymbol{k}-\boldsymbol{p}$ instead of $\sum_{\triangle_{kpq}}$ in (3.8). Then each triad is counted twice and $C^{s_k s_p s_q}_{\boldsymbol{kpq}}$ is replaced by $C^{s_k s_p s_q}_{\boldsymbol{kpq}}/2$.

In the limit $Ro \to 0$ ($\Omega \to \infty$), the triad interaction of (3.8) is maximal when the interaction is resonant, i.e. the wave frequencies satisfy the resonance condition

$$\sigma_{s_k}(\boldsymbol{k}) + \sigma_{s_p}(\boldsymbol{p}) + \sigma_{s_q}(\boldsymbol{q}) = 0. \tag{3.11}$$

Resonant triad interactions are not affected by fast rotation since the phase factor in (3.8) vanishes. The energy transfer of other triad interactions is, on average, reduced by the non-zero phase factor. With our choice of non-dimensional equations (3.1), the linear time scale is $O(Ro)$, and exactly resonant triad interactions dominate on time scales $O(1)$. The dispersion relation (3.5) allows resonant triad interactions, and the set of all wavevectors resonant with a given wavevector forms a two-dimensional manifold (a resonant trace) in three-dimensional Fourier space (e.g. the resonant trace for $\boldsymbol{k} = (4, 0, 8)$ is shown in figure 1 of Smith & Waleffe 1999). For a resonant triad $\triangle_{\boldsymbol{kpq}}$ with $k_z = 0$, the interaction coefficient $C_{\boldsymbol{kpq}}^{s_k s_p s_q} = 0$, so that the mode with wavevector $\boldsymbol{k} = (k_x, k_y, 0)$ cannot gain or lose energy directly through resonant triad interactions (Greenspan 1969; Waleffe 1993; Embid & Majda 1996; Babin *et al.* 1996, 2000). Note that modes with $k_z = 0$ correspond to z-independent two-dimensional modes and form a slow manifold with frequency $\sigma_s(\boldsymbol{k}) = 0$. For finite (small) Rossby numbers, near-resonant triad interactions are important on time scales $O(1/Ro)$, where near-resonant triads are defined by (3.11) with zero on the right-hand side replaced by $O(Ro)$ (see (3.13), Benney & Saffman 1966; Newell 1969; Zakharov *et al.* 1992).†

3.2. *Reduced models of three-dimensional rotating flow*

In numerical simulations with finite resolution, there is only a finite number of triad interactions in the numerical domain. Denoting the finite set of all triad interactions in the numerical domain by $\mathscr{I}_F$, the nonlinear term in (3.8) is replaced by the sum over all triads in $\mathscr{I}_F$, and is here denoted by $NL(\mathscr{I}_F)$. Generally, given a subset of triad interactions $\mathscr{I}$, the corresponding nonlinear term over all interactions in $\mathscr{I}$ is denoted by $NL(\mathscr{I})$:

$$NL(\mathscr{I}) = \sum_{\mathscr{I}} C_{\boldsymbol{kpq}}^{s_k s_p s_q} b_{s_p}^*(t; \boldsymbol{p}) b_{s_q}^*(t; \boldsymbol{q}) \exp\left[\mathrm{i}\big(\sigma_{s_k}(\boldsymbol{k}) + \sigma_{s_p}(\boldsymbol{p}) + \sigma_{s_q}(\boldsymbol{q})\big)\frac{t}{Ro}\right]. \tag{3.12}$$

For $\mathscr{I} \neq \mathscr{I}_F$ (so $\mathscr{I}$ is a proper subset of $\mathscr{I}_F$), the analogue of (3.8) obtained by replacing the nonlinear term $NL(\mathscr{I}_F)$ by $NL(\mathscr{I})$ is here referred to as a reduced model.

The role of near-resonant triad interactions is the main focus of this paper, and $\mathscr{I}_R(\epsilon; Ro)$ denotes the set of all triad interactions satisfying

$$|\sigma_{s_k}(\boldsymbol{k}) + \sigma_{s_p}(\boldsymbol{p}) + \sigma_{s_q}(\boldsymbol{q})| \leqslant \epsilon\ Ro \tag{3.13}$$

for positive $\epsilon = O(1)$. The two-dimensional dynamics among slow modes are also considered, and $\mathscr{I}_{2D}$ is the set of all two-dimensional triad interactions with $k_z = p_z = q_z = 0$. The corresponding reduced models are obtained by replacing the nonlinear term of (3.8) by $NL(\mathscr{I}_R(\epsilon; Ro))$ or $NL(\mathscr{I}_{2D})$, respectively. Note that in any reduced model, we keep all wave amplitudes (all the $b_s(t; \boldsymbol{k})$), but include a subset of triad interactions from the nonlinear term $NL(\mathscr{I}_F)$. For example, for a reduced model excluding triad interactions among two-dimensional modes, with the nonlinear

† In Newell (1969), the linear time scale is $O(1)$ and so the time scale for near-resonant triad interactions is $O(1/Ro^2)$.

term denoted $NL(\mathscr{I}) = NL(\mathscr{I}_F - \mathscr{I}_{2D})$, two-dimensional modes with $k_z = 0$ can gain or lose energy by interacting with non-two-dimensional modes having $k_z \neq 0$.

The quadratic nonlinearity in the discretized equations with nonlinear term $NL(\mathscr{I}_F)$ can be computed efficiently by the standard pseudo-spectral technique using fast Fourier transforms (FFTs) with e.g. the 2/3 rule for dealiasing (see e.g. Canuto *et al.* 1988; Boyd 2001). However, when the nonlinear term is modified to include only a subset of triads, the modified nonlinearity must be calculated directly in spectral space. Both time and storage costs for such direct calculations are very expensive, and thus numerical simulations of the reduced models are restricted to very low resolutions (our three-dimensional calculations use 64^3 Fourier modes). Computational time is the limiting factor. However, storage costs are also high if one saves the complex interaction coefficients $C_{\boldsymbol{kpq}}^{s_k s_p s_q}$. In the next section, we provide more specifics for our computations of reduced dynamics. The reader who is not interested in such details should proceed to § 5.

4. Direct calculation of the nonlinear interactions in wave space

4.1. *The strategy for a quadratic nonlinearity in two dimensions*

The direct calculation of the modified nonlinearity in reduced models requires (i) identifying the subset of triads to sum over, (ii) saving the subset and related quantities (for example, $s_{\boldsymbol{k}}$, $s_{\boldsymbol{p}}$, $s_{\boldsymbol{q}}$, $\boldsymbol{k}$, $\boldsymbol{p}$, $\boldsymbol{q}$ and the coefficients $C_{\boldsymbol{kpq}}^{s_k s_p s_q}$), and (iii) computing the sum directly in Fourier space. We discuss (i) and (iii) below.

For simplicity, we first consider a quadratic nonlinearity in two dimensions. The generalization to three-dimensional rotating flows is discussed in § 4.2. Let the quadratic nonlinearity be denoted

$$nl(\boldsymbol{k}) = \sum_{\triangle_{\boldsymbol{kpq}}} n(\boldsymbol{k}; \boldsymbol{p}, \boldsymbol{q}), \quad n(\boldsymbol{k}; \boldsymbol{p}, \boldsymbol{q}) = C_{\boldsymbol{kpq}} b^*(\boldsymbol{p}) b^*(\boldsymbol{q}), \tag{4.1}$$

where the vectors $\boldsymbol{k}$, $\boldsymbol{p}$, $\boldsymbol{q}$ are two-dimensional vectors. The expression $n(\boldsymbol{k}; \boldsymbol{p}, \boldsymbol{q})$ is the nonlinear contribution to $\boldsymbol{k}$ through the triad interaction among $\boldsymbol{k}$, $\boldsymbol{p}$, and $\boldsymbol{q}$; $nl(\boldsymbol{k})$ is the total nonlinear contribution to $\boldsymbol{k}$ obtained by summing over all $\boldsymbol{p}$ and $\boldsymbol{q}$; $b(\boldsymbol{k})$ and $C_{\boldsymbol{kpq}}$ are generic two-dimensional analogues of $b_{s_k}(\boldsymbol{k})$ and $C_{\boldsymbol{kpq}}^{s_k s_p s_q}$ in (3.8). The wave amplitudes $b(\boldsymbol{k})$ and coupling coefficients $C_{\boldsymbol{kpq}}$ are assumed to satisfy the reality conditions (i) $b(\boldsymbol{k}) = b^*(-\boldsymbol{k})$ and (ii) $C_{\boldsymbol{kpq}} = C^*_{-\boldsymbol{k},-\boldsymbol{p},-\boldsymbol{q}}$. We also assume that (iii) $C_{\boldsymbol{kpq}} = 0$ if $\boldsymbol{k}$, $\boldsymbol{p}$ and $\boldsymbol{q}$ are collinear, and (iv) $C_{\boldsymbol{kpq}} = C_{\boldsymbol{kqp}}$ (so that $n(\boldsymbol{k}; \boldsymbol{p}, \boldsymbol{q}) = n(\boldsymbol{k}; \boldsymbol{q}, \boldsymbol{p})$). Note that the nonlinear interactions for three-dimensional rotating flows satisfy the three-dimensional analogues of these assumptions (Waleffe 1992). With the third assumption, the sum in (4.1) can be restricted to non-collinear triads.

For the pseudo-spectral method over a two-dimensional periodic square, the domain of wavevectors for an isotropic grid in Fourier space is

$$K^+ = \{\boldsymbol{k} = (j_x, j_y)\Delta k\} \begin{cases} \text{either } j_x = 0 \quad \text{and} \quad j_y = 1, 2, \ldots, M \\ \text{or } j_x = 1, 2, \ldots, M \quad \text{and} \quad j_y = -M, -M+1, \ldots, M \end{cases} \tag{4.2}$$

where Δk is the distance between two adjacent wavevectors and M is a positive integer (Canuto *et al.* 1988; Boyd 2001). The region K^+ is the right-hand grey area in figure 1, and $K^- = -K^+ = \{\boldsymbol{k} : -\boldsymbol{k} \in K^+\}$. As a consequence of the reality conditions on $b(\boldsymbol{k})$ and $C_{\boldsymbol{kpq}}$, only information in K^+ is needed to construct the wave field over the entire

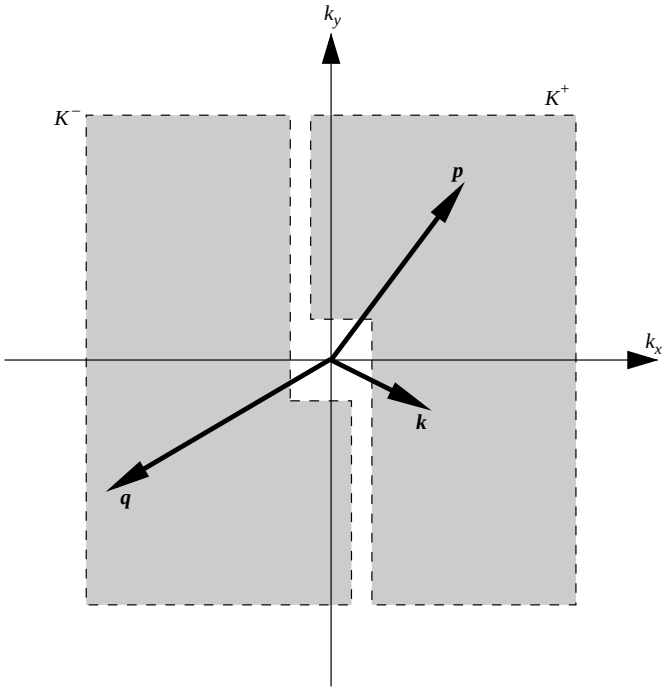

FIGURE 1. K^+ is the domain in Fourier space for the pseudo-spectral method. The triad $\triangle_{\boldsymbol{kpq}}$ is in T^+ with $\boldsymbol{k} < \boldsymbol{p}$.

square $K^+ \cup K^-$. Note that M is usually chosen as one third of the resolution size to avoid aliasing by using the so-called 2/3 rule.

Let T^+ be the set of all non-collinear triads with two wavevectors in K^+ and the remaining wavevector in K^-. For example, the triad in figure 1 is in T^+ because $\boldsymbol{k}, \boldsymbol{p} \in K^+$ and $\boldsymbol{q} \in K^-$. Let T^- be the set of triads whose Fourier conjugate is in T^+: $T^- = \{\triangle_{\boldsymbol{kpq}} : \triangle_{-\boldsymbol{k},-\boldsymbol{p},-\boldsymbol{q}} \in T^+\}$. So, any triad in T^- has two wavevectors in K^- and the remaining wavevector in K^+. Since any non-collinear triad is in either T^+ or T^-, the sum for the full nonlinearity in (4.1) is taken over $T^+ \cup T^-$.

For T, a given subset of $T^+ \cup T^-$, we now describe a numerical procedure to compute the nonlinear interactions over T. For fixed triad $\triangle_{\boldsymbol{kpq}}$ in $T \cap T^+$, without loss of generality, $\boldsymbol{k}$ and $\boldsymbol{p}$ are in K^+ and $\boldsymbol{q}$ is in K^-. Since we need only mode amplitudes $b(\boldsymbol{k})$, $b(\boldsymbol{p})$ and $b(-\boldsymbol{q})$ with wavevectors in K^+, then we need only compute the nonlinear terms $n(\boldsymbol{k};\boldsymbol{p},\boldsymbol{q}) = n(\boldsymbol{k};\boldsymbol{q},\boldsymbol{p})$, $n(\boldsymbol{p};\boldsymbol{q},\boldsymbol{k}) = n(\boldsymbol{p};\boldsymbol{k},\boldsymbol{q})$, and $n(-\boldsymbol{q};-\boldsymbol{k},-\boldsymbol{p}) = n(-\boldsymbol{q};-\boldsymbol{p},-\boldsymbol{k})$. Note that $n(\boldsymbol{q};\boldsymbol{k},\boldsymbol{p})$ is not needed because $\boldsymbol{q}$ is not in the computation domain K^+. However, its conjugate $n(-\boldsymbol{q};-\boldsymbol{k},-\boldsymbol{p})$ must be computed because $-\boldsymbol{q}$ is in K^+. Using (4.1) and the reality condition for $b(\boldsymbol{k})$, the nonlinear interactions $n(\boldsymbol{k};\boldsymbol{p},\boldsymbol{q})$ and $n(\boldsymbol{p};\boldsymbol{q},\boldsymbol{k})$ are computed as

$$\left.\begin{aligned} n(\boldsymbol{k};\boldsymbol{p},\boldsymbol{q}) &= C_{\boldsymbol{kpq}} b^*(\boldsymbol{p}) b(-\boldsymbol{q}), \\ n(\boldsymbol{p};\boldsymbol{q},\boldsymbol{k}) &= C_{\boldsymbol{pqk}} b(-\boldsymbol{q}) b^*(\boldsymbol{k}), \end{aligned}\right\} \tag{4.3}$$

where $b^*(\boldsymbol{q})$ is computed using $b(-\boldsymbol{q})$ since $\boldsymbol{q}$ is not in the computation domain K^+. Finally, $n(-\boldsymbol{q};-\boldsymbol{k},-\boldsymbol{p})$ is computed using reality of $C_{\boldsymbol{kpq}}$ and the conjugate triad $\triangle_{-\boldsymbol{k},-\boldsymbol{p},-\boldsymbol{q}}$:

$$n(-\boldsymbol{q};-\boldsymbol{k},-\boldsymbol{p}) = C^*_{\boldsymbol{qkp}} b(\boldsymbol{k}) b(\boldsymbol{p}). \tag{4.4}$$

Again, amplitudes $b(\boldsymbol{k})$ and $b(\boldsymbol{p})$ with wavevectors in K^+ are used for amplitudes $b^*(-\boldsymbol{k})$ and $b^*(-\boldsymbol{p})$ with wavevectors in K^-, respectively. Expressions (4.3) and (4.4) are combined to compute the nonlinear interactions for the triad $\triangle_{\boldsymbol{kpq}}$ and its conjugate triad $\triangle_{-\boldsymbol{k},-\boldsymbol{p},-\boldsymbol{q}}$, using only modes with wavevectors in K^+ ($b(\boldsymbol{k})$, $b(\boldsymbol{p})$, and $b(-\boldsymbol{q})$).

It remains to discuss how to identify the triads in T, and it is enough to find the triads in $T \cap T^+$ because of the reality conditions. This requires a systematic procedure to search over all triads in T^+. For this purpose, an order is introduced between wavevectors in K^+:

$$\boldsymbol{k} < \boldsymbol{p} \quad \text{if either} \quad k_x < p_x, \quad \text{or} \quad k_x = p_x, k_y < p_y. \tag{4.5}$$

Then, for each triad $\triangle_{\boldsymbol{kpq}}$ in T^+ and without loss of generality, one can assume that $\boldsymbol{k}$ and $\boldsymbol{p}$ are in K^+ with $\boldsymbol{k} < \boldsymbol{p}$ and $\boldsymbol{q} = -\boldsymbol{k} - \boldsymbol{p}$ (e.g. see the triad in figure 1). The procedure to span T^+ is now straightforward: for each $\boldsymbol{k}$ in K^+, loop over all $\boldsymbol{p}$ in K^+ with $\boldsymbol{p} > \boldsymbol{k}$. If the triad $\triangle_{\boldsymbol{kpq}}$ in T^+ is also an element of T, then store the triad and its interaction coefficients.

- for each $\boldsymbol{k} \in K^+$,
  - for each $\boldsymbol{p} \in K^+$ and $\boldsymbol{p} > \boldsymbol{k}$,
    - — Let $\boldsymbol{q} = -\boldsymbol{k} - \boldsymbol{p}$.
    - — Check $\triangle_{\boldsymbol{k},\boldsymbol{p},\boldsymbol{q}} \in T$.
      - – if yes, store $\triangle_{\boldsymbol{k},\boldsymbol{p},\boldsymbol{q}}$, and its interaction coefficients
  - end of $\boldsymbol{p}$ for-loop
- end of $\boldsymbol{k}$ for-loop

Note that if $\boldsymbol{p} = \boldsymbol{k}$, then the triad $\triangle_{\boldsymbol{kpq}}$ is collinear, and the nonlinear interactions among the triad are identically zero. Thus, it is sufficient to consider $\boldsymbol{p}$ that is strictly greater than $\boldsymbol{k}$.

4.2. *Extension to three-dimensional rotating flows*

Below we extend the ideas of the previous section to compute the nonlinear interactions directly in three-dimensional rotating flows. To this end, it is convenient to represent both the velocity $\boldsymbol{u}$ and the nonlinear term $\boldsymbol{u} \times (\nabla \times \boldsymbol{u})$ as a sum of helical modes

$$\left.\begin{aligned} \boldsymbol{u}(\boldsymbol{x}, t) &= \sum_{\boldsymbol{k}} \sum_{s} a_s(t; \boldsymbol{k}) \boldsymbol{h}_s(\boldsymbol{k}) \exp(\mathrm{i}\boldsymbol{k} \cdot \boldsymbol{x}), \\ (\boldsymbol{u} \times (\nabla \times \boldsymbol{u}))(\boldsymbol{x}, t) &= \sum_{\boldsymbol{k}} \sum_{s} nl_s(t; \boldsymbol{k}) \boldsymbol{h}_s(\boldsymbol{k}) \exp(\mathrm{i}\boldsymbol{k} \cdot \boldsymbol{x}). \end{aligned}\right\} \tag{4.6}$$

Here, $a_s(t; \boldsymbol{k}) = b_s(t; \boldsymbol{k}) \exp(-\mathrm{i}\sigma_s(\boldsymbol{k}) t / Ro)$ includes the phase factor (see (3.7)). Then, the nonlinear interaction $nl_{s_k}(t; \boldsymbol{k})$ reads

$$\left.\begin{aligned} nl_{s_k}(t; \boldsymbol{k}) &= \sum_{\triangle_{\boldsymbol{kpq}}} \sum_{s_p, s_q = \pm 1} n(\boldsymbol{k}, s_k; \boldsymbol{p}, s_p, \boldsymbol{q}, s_q), \\ n(\boldsymbol{k}, s_k; \boldsymbol{p}, s_p, \boldsymbol{q}, s_q) &= C_{\boldsymbol{kpq}}^{s_k s_p s_q} a_{s_p}^*(t; \boldsymbol{p}) a_{s_q}^*(t; \boldsymbol{q}) \end{aligned}\right\} \tag{4.7}$$

where the coefficient $C_{\boldsymbol{kpq}}^{s_k s_p s_q}$ is given by (3.9).

For three-dimensional flows, K^+ corresponds to the set of wavevectors $\boldsymbol{k}$ with either (i) $k_x > 0$, (ii) $k_x = 0$ and $k_y > 0$, or (iii) $k_x = k_y = 0$ and $k_z > 0$. As above in § 4.1, first consider a fixed triad $\triangle_{\boldsymbol{kpq}}$ with $\boldsymbol{k}$ and $\boldsymbol{p}$ in K^+. Similar to (4.3) and (4.4), the

(s_k, s_p, s_q)-type nonlinear interactions at $\boldsymbol{k}$, $\boldsymbol{p}$, and $-\boldsymbol{q}$ are computed by

$$\left.\begin{aligned} n(\boldsymbol{k}, s_k; \boldsymbol{p}, s_p, \boldsymbol{q}, s_q) &= C^{s_k s_p s_q}_{\boldsymbol{k p q}} a^*_{s_p}(\boldsymbol{p}) a_{s_q}(-\boldsymbol{q}) \\ n(\boldsymbol{p}, s_p; \boldsymbol{q}, s_q, \boldsymbol{k}, s_k) &= C^{s_p s_q s_k}_{\boldsymbol{p q k}} a_{s_q}(-\boldsymbol{q}) a^*_{s_k}(\boldsymbol{k}) \\ n(-\boldsymbol{q}, s_p; -\boldsymbol{k}, s_k, -\boldsymbol{p}, s_p) &= \left[C^{s_q s_k s_p}_{\boldsymbol{q k p}}\right]^* a_{s_k}(\boldsymbol{k}) a_{s_p}(\boldsymbol{p}). \end{aligned}\right\} \tag{4.8}$$

Once the interaction coefficients $C^{s_k s_p s_q}_{\boldsymbol{k p q}}$, $C^{s_p s_q s_k}_{\boldsymbol{p q k}}$, and $C^{s_q s_k s_p}_{\boldsymbol{q k p}}$ are computed, the second property of (3.10*b*) allows one to compute the $(-s_k, -s_p, -s_q)$-type nonlinear interactions as

$$\left.\begin{aligned} n(\boldsymbol{k}, -s_k; \boldsymbol{p}, -s_p, \boldsymbol{q}, -s_q) &= -\left[C^{s_k s_p s_q}_{\boldsymbol{k p q}}\right]^* a^*_{-s_p}(\boldsymbol{p}) a_{-s_q}(-\boldsymbol{q}) \\ n(\boldsymbol{p}, -s_p; \boldsymbol{q}, -s_q, \boldsymbol{k}, -s_k) &= -\left[C^{s_p s_q s_k}_{\boldsymbol{p q k}}\right]^* a_{-s_q}(-\boldsymbol{q}) a^*_{-s_k}(\boldsymbol{k}) \\ n(-\boldsymbol{q}, -s_p; -\boldsymbol{k}, -s_k, -\boldsymbol{p}, -s_p) &= -C^{s_q s_k s_p}_{\boldsymbol{q k p}} a_{-s_k}(\boldsymbol{k}) a_{-s_p}(\boldsymbol{p}). \end{aligned}\right\} \tag{4.9}$$

For example, if the (s_k, s_p, s_q)-type interaction of a triad $\triangle_{\boldsymbol{k},\boldsymbol{p},\boldsymbol{q}}$ is near-resonant, then the $(-s_k, -s_p, -s_q)$-type interaction is also near-resonant, and (4.9) allows one to compute the $(-s_k, -s_p, -s_q)$-type interaction without explicitly computing $C^{-s_k,-s_p,-s_q}_{\boldsymbol{k p q}}$, $C^{-s_p,-s_q,-s_k}_{\boldsymbol{p q k}}$, and $C^{-s_q,-s_k,-s_p}_{\boldsymbol{q k p}}$. Finally, one may order wavevectors in T^+ as

$$\boldsymbol{k} < \boldsymbol{p} \text{ if either } k_x < p_x, \text{ or } k_x = p_x,\ k_y < p_y, \text{ or } k_x = p_x,\ k_y = p_y,\ k_z < p_z,$$

and span T^+ by looping over all $\boldsymbol{p}$ in K^+ with $\boldsymbol{p} > \boldsymbol{k}$.

As a simple test, we calculated the inviscid, unforced dynamics of $(+,+,+)$-type and $(-,-,-)$-type interactions for the resonant triad $\boldsymbol{k} = (4, 0, 8)$, $\boldsymbol{p} = (6, 0, -3)$, and $\boldsymbol{q} = (-10, 0, -5)$, and for frame rotation rate $\Omega = 1$. In other words, the full nonlinear term is replaced by $NL(\mathscr{I})$ with

$$\mathscr{I} = \{(+,+,+)\text{-type and } (-,-,-)\text{-type interactions among } \boldsymbol{k},\ \boldsymbol{p}, \text{ and } \boldsymbol{q} \text{ fixed}\}.$$

In figure 2, the solid lines are the real (a) and imaginary (b) parts of amplitudes $b_+(\boldsymbol{k})$, $b_+(\boldsymbol{p})$, and $b_+(\boldsymbol{q})$ from numerical simulation of the reduced model with $NL(\mathscr{I})$. The code is based on the dimensional versions of (3.1), (3.7)–(3.9), with full nonlinearity replaced by the dimensional version of (3.12). In figure 2, we plot the dimensional time and amplitudes b_+, where the dimensions of b_+ are length/time. Since the $(+,+,+)$-type interaction is decoupled from the $(-,-,-)$-type interaction, the amplitudes $b_+(\boldsymbol{k})$, $b_+(\boldsymbol{p})$, and $b_+(\boldsymbol{q})$ are governed by the triad system

$$\left.\begin{aligned} \partial_t b_+(\boldsymbol{k}) &= C^{+++}_{\boldsymbol{k p q}} b^*_+(\boldsymbol{p}) b^*_+(\boldsymbol{q}), \\ \partial_t b_+(\boldsymbol{p}) &= C^{+++}_{\boldsymbol{p q k}} b^*_+(\boldsymbol{q}) b^*_+(\boldsymbol{k}), \\ \partial_t b_+(\boldsymbol{q}) &= C^{+++}_{\boldsymbol{q k p}} b^*_+(\boldsymbol{k}) b^*_+(\boldsymbol{p}). \end{aligned}\right\} \tag{4.10}$$

Equations (4.10) are solved independently using the same initial conditions as the reduced model, and the amplitudes are plotted using symbols in figure 2. One can see that the results of the reduced model calculation match the results of solving (4.10).

5. Numerical results

As mentioned above, the numerical codes are based on the dimensional versions of (3.1), (3.7)–(3.9) and (3.12). The Fourier transform of the momentum equation with full nonlinear term $NL(\mathscr{I}_F)$ or modified nonlinear term $NL(\mathscr{I})$ is integrated forward in time using the third-order Runge–Kutta time-stepping scheme. For all calculations,

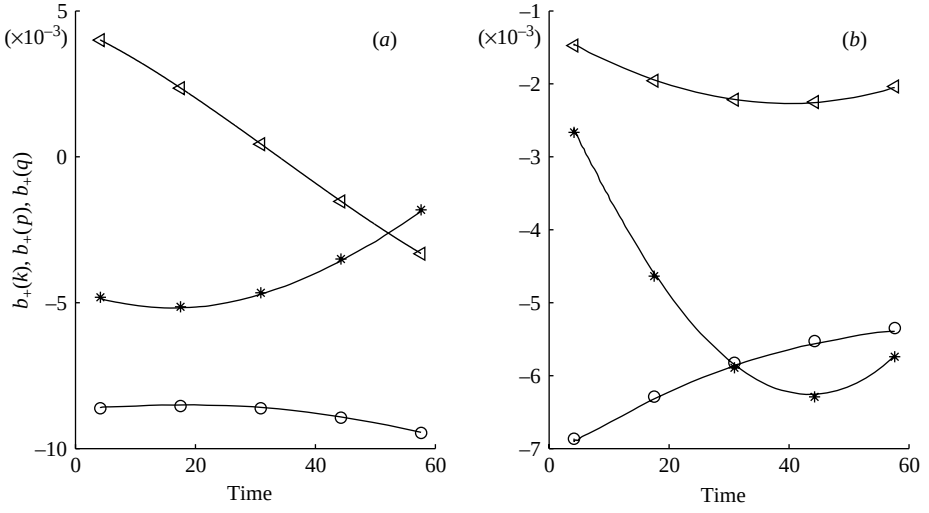

FIGURE 2. A test case: the nonlinear term is modified to include only two interactions: $(+,+,+)$-type and $(-,-,-)$-type interactions among $\boldsymbol{k}=(4,0,8)$, $\boldsymbol{p}=(6,0,-3)$, and $\boldsymbol{q}=(-10,0,-5)$. (*a*) and (*b*) Respectively, the real and imaginary parts of $b_+(\boldsymbol{k})$ (star), $b_+(\boldsymbol{p})$ (circle), and $b_+(\boldsymbol{q})$ (triangle). Solid lines are computed using (4.7)–(4.9). Symbols are computed from (4.10).

the physical domain is a triply periodic cube with volume $(2\pi)^3$, and the initial velocity is $\boldsymbol{u}(\boldsymbol{x},t)=0$. Incompressibility is enforced at each time step by projection onto the (incompressible) linear eigenmodes (3.4) (see Smith & Waleffe 2002). The linear wave and viscosity terms are treated using an integrating factor technique. The nonlinear interactions $NL(\mathscr{I}_F)$ are calculated in physical space using FFTs, while the nonlinear interactions of reduced dynamics are computed directly in Fourier space using the procedure discussed in § 4.

Following Smith & Waleffe (1999), at times $t>0$, a white noise force adds energy at an average rate $\varepsilon_f \approx 1$. The forcing spectrum $F(k)$ is Gaussian with peak wavenumber k_f and standard deviation $\sigma=1$, given by

$$F(k)=\varepsilon_f \frac{\exp(-0.5(k-k_f)^2/\sigma^2)}{(2\pi)^{1/2}\sigma}. \tag{5.1}$$

The dissipation at small scales is modelled by a hyperviscosity term $-\nu_H\nabla^{2p_H}$ with $p_H=8$ in place of the normal viscosity term $\nu\nabla^2$. The purpose of using hyperviscosity, which turns on much more abruptly than the gradual increase of normal viscosity at small scales, is to eliminate as much as possible the effects of viscosity at intermediate scales, thus extending the turbulence inertial range(s). The numerical simulations are characterized by the following Rossby number Ro and Reynolds number Re_H:

$$Ro=\frac{\left(\varepsilon_f k_f^2\right)^{1/3}}{2\Omega}, \quad Re_H=\frac{\left(\varepsilon_f k_f^2\right)^{1/3}}{\nu_H k_f^{2p_H}}. \tag{5.2}$$

These expressions are obtained by using the length scale $L=k_f^{-1}$, velocity scale $U=(\varepsilon_f/k_f)^{1/3}$ and time scale $L/U=(\varepsilon_f k_f^2)^{-1/3}$ in (3.2). Here we present simulation results of full and reduced dynamics using dimensional parameter values $k_f=10$, $\varepsilon_f\approx 0.7$, and $\Omega=24$, with corresponding Rossby number $Ro=0.086$. We use a dynamic hyperviscosity given by $\nu_H=\gamma(E(k_{\max})/k_{\max})^{1/2}k_{\max}^{2-2p_H}$, where $E(k_{\max})$ is the energy in

the highest wavenumber shell. The maximum wavenumber $k_{\max}$ is given by $k_{\max} = N/3$ for resolution N^3 and dealiasing using the 2/3 rule. In such a scheme, the non-dimensional proportionality coefficient γ is usually taken to be approximately one, and is arbitrarily set to $\gamma = 2.5$ in our code. At the beginning of each run, $E(k_{\max})$ and ν_H grow until statistical stationarity is established for wavenumbers higher than the forcing wavenumbers. Then the energy dissipation rate $\varepsilon^> \equiv \nu_H \sum_k k^{2p_H} E(k)$ is also statistically steady. For the full simulation with $N = 64$, ν_H and $\varepsilon^>$ grow to the average values $\nu_H \approx 1.1 \times 10^{-20}$ and $\varepsilon^> \approx 0.53$, giving a dissipation wavenumber $k_d \equiv (\varepsilon^>/\nu_H^3)^{1/46} \approx 19.8$ (see figure 3).

In the following sections, we present four types of plot: (i) energy spectra vs. wavenumber, (ii) total energy in large scales with $0 \leqslant k \leqslant 5$ vs. time, (iii) contours of the vertical vorticity corresponding to the vertically averaged velocity field (in the (x, y)-plane), and (iv) probability density functions (PDFs) of vertical vorticity in vertically averaged velocity fields. On plots of energy spectra, all wavenumbers and spectra are left dimensional for ease of locating the forcing wavenumber $k_f = 10$ and the dissipation wavenumber $k_d \approx 19.8$ (see figure 3). On all other plots, time is scaled by $(\varepsilon_f k_f^2)^{-1/3}$, total energy is scaled by $(\varepsilon_f/k_f)^{2/3}$, and vorticity is scaled by $f = 2\Omega$.

5.1. *Energy transfer into two-dimensional large-scale motions*

For large Rossby numbers (weak rotation), the results of 128^3 and 200^3 simulations show that energy input from three-dimensional isotropic forcing is transferred to smaller scales and dissipated by viscosity. However, if the Rossby number is smaller than an $O(1)$ critical value, energy is transferred to scales larger than the forced scales (Smith & Waleffe 1999, see also Hossain 1994). For moderately small values of the Rossby number below critical, three important features of the flow are (i) the generation of two-dimensional large scales from three-dimensional forcing, (ii) a large-scale two-dimensional energy spectrum scaling close to $E(k_h; k_z = 0) \propto k_h^{-3}$, and (iii) the dominance of cyclonic vortices. The large-scale spectrum $E(k_h; k_z = 0) \propto k_h^{-3}$ of the three-dimensional rotating flow is steeper than the two-dimensional spectrum $E(k_h) \propto k_h^{-5/3}$ associated with the energy range in isotropic two-dimensional two-component turbulence (Kraichnan 1967; see also Smith & Yakhot 1994). As previously mentioned, all reduced models are restricted to low resolution (64^3 Fourier modes) by the time cost of direct spectral calculation of the quadratic nonlinearity. For a fair comparison, the full equations with nonlinearity $NL(\mathscr{I}_F)$ are simulated with resolution 64^3 to establish that the above three features of the large-scale flow are captured with lower resolution (figures 3–6).

Figure 3 compares energy spectra for the full simulation with resolution 64^3 Fourier modes at Rossby number $Ro = 0.085$. The time $t = 69$ is toward the end of the simulation. Since we do not use large-scale dissipation, we stop all simulations when energy has populated the lowest wavenumber $k = 1$, but before energy has accumulated in $k = 1$ above the level consistent with scaling $E_0(k_h) \equiv E(k_h; k_z = 0) \propto k_h^{-3}$ (or $E_0(k_h) \propto k_h^{-5/3}$ for the reduced model including only two-dimensional interactions). All results shown here are insensitive to the exact stopping time. The shell-integrated spectrum $E(k)$ (solid line) is obtained by summing the energy of all modes with wavenumber in the three-dimensional shell $[k - \Delta k/2, k + \Delta k/2]$, where $k = (k_x^2 + k_y^2 + k_z^2)^{1/2}$. The spectrum $E_0(k_h) \equiv E(k_h; k_z = 0)$ (dashed line) is the energy spectrum of modes with no vertical variation, obtained by summing over modes with vertical wavenumber $k_z = 0$ and horizontal wavenumber k_h in the two-dimensional shell $[k_h - \Delta k_h/2, k_h + \Delta k_h/2]$, where $k_h = \sqrt{k_x^2 + k_y^2}$. The total energy E can be found by summing over all k: $E = \sum_k E(k)$, or equivalently $E = \sum_{k_h} \sum_{k_z} E(k_h, k_z)$. In most

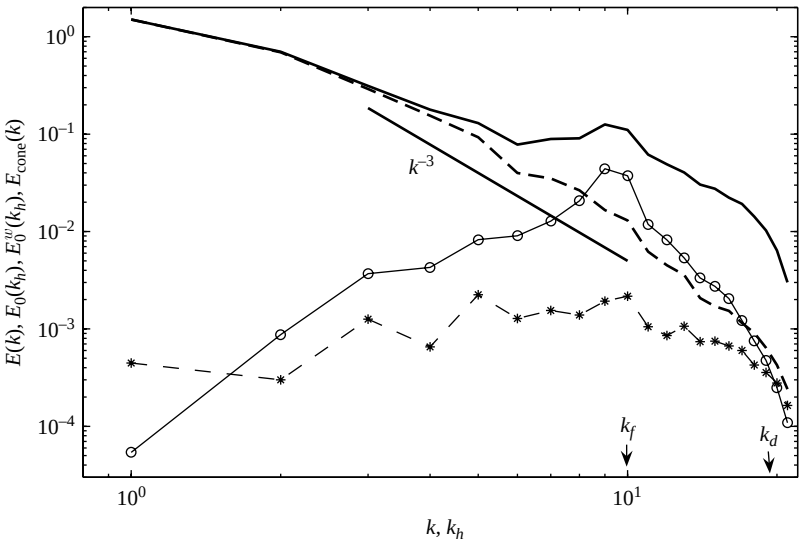

FIGURE 3. Energy spectra for the full simulation at time $t = 69$ (resolution 64^3 Fourier modes). The solid curve is the three-dimensional energy spectrum $E(k)$ and the dashed curve is the two-dimensional energy spectrum $E_0(k_h) \equiv E(k_h; k_z = 0)$. The dashed line with stars is the energy spectrum $E_0^w(k_h) \equiv E^w(k_h; k_z = 0)$ corresponding to the vertical component of velocity with $k_z = 0$. The solid line with circles is the energy spectrum $E_{\rm cone}(k)$ corresponding to modes with wavevector in the cone defined by $k_h/|k_z| < 1$.

figures, we plot $E(k_h, k_z)$ for one value of k_z, namely $k_z = 0$, since the modes with $k_z = 0$ contain almost all of the large-scale energy at long times in the 128^3 and 200^3 simulations, and the modes with $k_z \neq 0$ contained negligible energy at scales larger than the forcing scales (Smith & Waleffe 1999). In figure 3, a comparison between $E(k)$ (solid) and $E_0(k_h) = E(k_h; k_z = 0)$ (dashed) shows again that the large scale energy is in two-dimensional modes with $k_z = 0$, while the small scale energy is in three-dimensional modes, where large scale and small scale are relative to the forced scales. In figure 3, we also plot the spectrum of the vertical component of velocity with $k_z = 0$, $E_0^w(k_h) \equiv E^w(k_h; k_z = 0)$ (dashed line with stars). The low energy level of $E_0^w(k_h)$ compared to $E_0(k_h)$ (the energy spectrum of all velocity components with $k_z = 0$) shows that most of the large-scale flow is not only two-dimensional, but also two-component, with energy predominantly in the horizontal velocity components with $k_z = 0$. The fourth spectrum on figure 3, denoted $E_{\rm cone}(k)$ (solid line with circles), is the spectrum of modes with wavevectors in the cone $k_h/|k_z| < 1$ about the $\hat{\mathbf{z}}$-axis. The low level of $E_{\rm cone}(k)$ compared to $E_0(k_h)$ at large scales highlights the dominance of large-scale two-dimensional modes as compared to modes with strong vertical variation. Recall that the horizontal modes having $k_z = 0$ cannot receive energy by exactly resonant interactions with three-dimensional modes having $k_z \neq 0$, but our results show that $k_z = 0$ modes do receive energy from near-resonant interactions in simulations at moderate Rossby number (see § 5.1.1). Thus the $k_z = 0$ modes are more dominant in our simulations than in the weak turbulence and closure theories (Galtier 2003; Cambon *et al.* 2004).

Figure 4 compares $E(k)$ (solid) and $E_0(k_h) \equiv E(k_h; k_z = 0)$ (dashed) for the three-dimensional rotating flow to the two-dimensional energy spectrum $E_0(k_h)$ (dashed) for the reduced model including only two-dimensional interactions ($\mathscr{I}_{2D}$). The latter reflects the isotropic two-dimensional inverse cascade. A k^{-3} line is also shown for reference. The transfer of energy to large scales by purely two-dimensional interactions

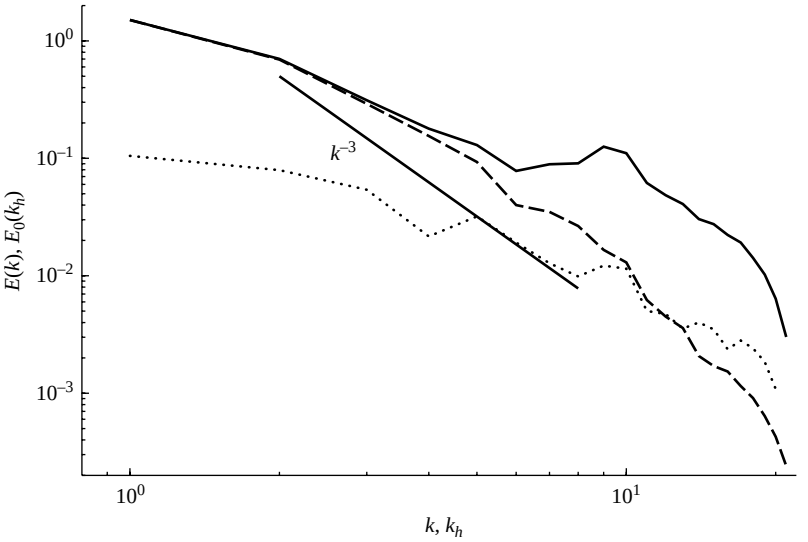

FIGURE 4. Energy spectra for the full simulation at time $t = 69$ (resolution 64^3 Fourier modes). The solid curve is the three-dimensional energy spectrum $E(k)$ and the dashed curve is the two-dimensional energy spectrum $E_0(k_h) \equiv E(k_h; k_z = 0)$. The lower dotted curve is the two-dimensional energy spectrum $E_0(k_h)$ at time $t = 105$ for the reduced model including only two-dimensional interactions, reflecting the isotropic two-dimensional inverse cascade.

is dramatically slower than in the full simulation including all interactions (figure 7). Thus we have chosen to plot the spectrum for purely two-dimensional interactions at the later time $t = 105$, when a comparable number of low-wavenumber modes has been populated, so that the difference in spectral steepness is more obvious. Even at the low resolution of 64^3 Fourier modes, it is clear that the large-scale two-dimensional modes of the three-dimensional rotating flow have more energy and a steeper spectrum than the large-scale two-dimensional modes of the purely two-dimensional flow.

Figure 5 shows contours of the vertical vorticity for the vertically averaged velocity, obtained by filtering out three-dimensional modes with $k_z \neq 0$, or equivalently by averaging over z. Figure 6 shows the PDF of vertical vorticity in the $\hat{\mathbf{z}}$-averaged velocity field at times $t = 35$ and $t = 69$ (the latter time matches the spectra of figure 4 and the physical space figure 5). The vortex regions have been identified using the criterion $Q = u_x v_y - u_y v_x > 0$ for a vortex region in two dimensions (see Jeong & Hussain 1995 and references therein). Here all PDFs are sampled over points (x, y) with $Q(x, y) > (1/4) \max Q$. MATLAB subroutine 'ksdensity' with the smoothing factor 0.02 is used to generate all PDFs.

One sees that all the important features of the higher-resolution simulations are observed in figures 3–6, corresponding to 64^3 Fourier modes. Thus we are confident that study of reduced models, even at low resolution of 64^3 Fourier modes, can give insight into the mechanisms responsible for anisotropic energy transfer from isotropic three-dimensional small-scale fluctuations to two-dimensional large-scale cyclonic vortical columns.

5.1.1. *Near-resonant and non-resonant triad interactions*

Although resonant triad interactions cannot transfer energy directly from wave modes to slow two-dimensional modes with $k_z = 0$, they may indirectly play an

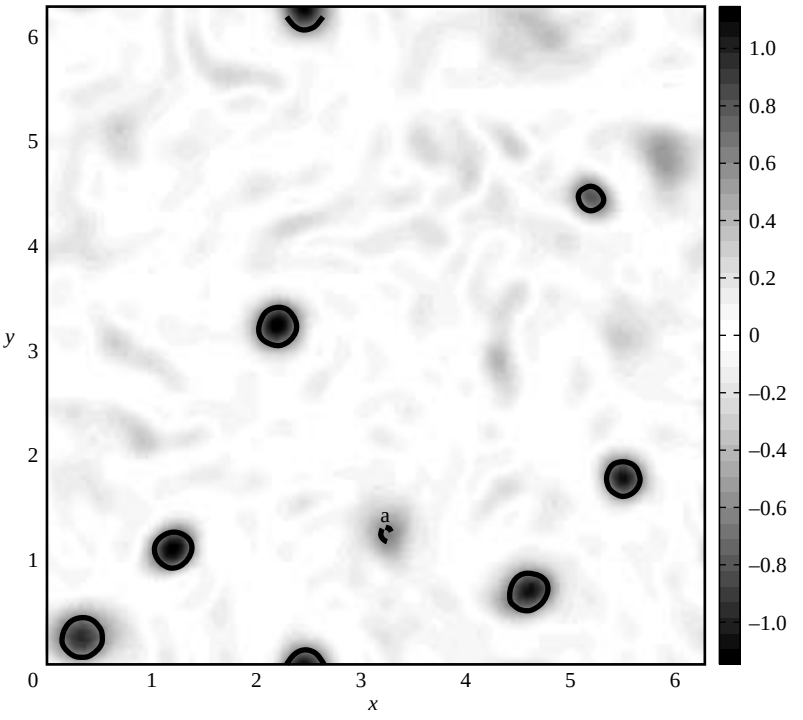

FIGURE 5. Contours of the vertical vorticity of the $\hat{\mathbf{z}}$-averaged velocity at $t = 69$ for the full simulation. Black indicates strong vorticity, and cyclones (anticyclones) are encircled by solid (dashed) contours. Anticyclones are also labelled by the letter a.

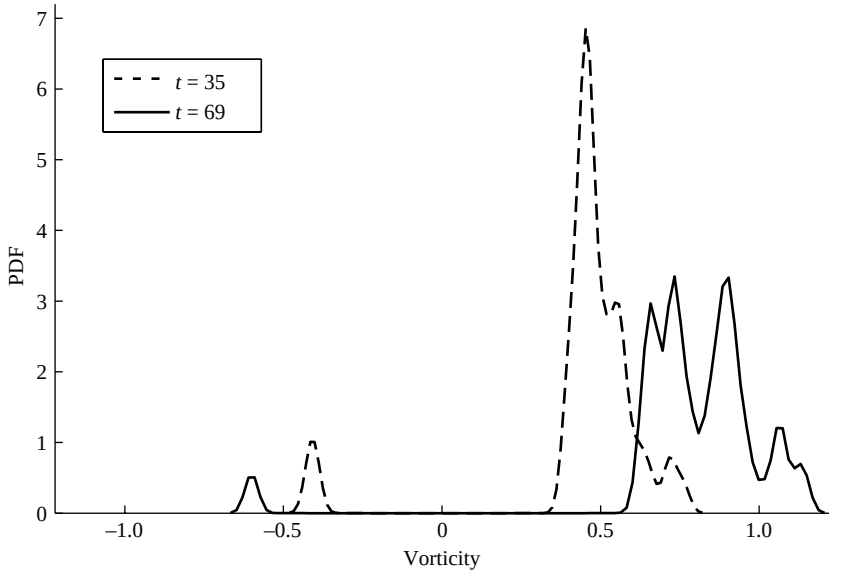

FIGURE 6. PDF of vertical vorticity in the $\hat{\mathbf{z}}$-averaged velocity field at $t = 35$ and $t = 69$ for the full simulation.

important role in the generation of large-scale two-dimensional modes. Analysis of a single resonant triad with one forced mode shows that resonant triads transfer energy toward smaller $|k_z|/k$ (Smith & Waleffe 1999; Majda, Timofeyev & Vanden-Eijnden 1999, 2001; see also Waleffe 1993). It is important to note that resonant traces are two-dimensional manifolds with measure zero in infinite resolution, and that on any finite grid, there are few exact three-dimensional resonant triad interactions, and even fewer with three non-zero coupling coefficients $C_{\boldsymbol{kpq}}^{s_k s_p s_q}$, $C_{\boldsymbol{pqk}}^{s_p s_q s_k}$, and $C_{\boldsymbol{qkp}}^{s_q s_k s_p}$. In a three-dimensional triad, two of the wavevectors lie out of the horizontal plane ($k_z = 0$). For our simulation grid, there are 77 243 296 triads, and thus the number of all triad interactions is $77\,243\,296 \times 8 = 617\,946\,368$, since there are eight types of interactions depending on the mode helicities. There are only 2152 $\pm(+,+,+)$-type, 96 $\pm(+,+,-)$-type , 68 $\pm(+,-,+)$-type, and 28 $\pm(+,-,-)$-type three-dimensional exact resonant interactions between modes with three-dimensional wavevectors. Thus the total number of such interactions is 4688, including all helicity combinations, or only $7.5 \times 10^{-4}\%$ of all triad interactions. Of these 4688 exact three-dimensional resonant interactions, only 264 have all three non-zero coupling coefficients; many correspond to equilateral triangles with all zero coupling coefficients, and some others correspond to resonant triads with one two-dimensional leg, and zero coupling coefficient for the two-dimensional mode. The numbers above are calculated numerically by looping over wavevectors as described in § 4. If the sum of frequencies for a triad is sufficiently small, the condition for exact resonance is tested analytically.

Exactly resonant interactions dominate for $Ro \to 0.1$; however in the present study, we consider Rossby numbers $Ro \approx 0.1$. For these Rossby numbers, numerical and laboratory experiments suggest that near-resonant triad interactions and/or higher-order resonant interactions are relevant (see § 1). Near-resonant triads are defined by (3.13) with $\epsilon = O(1)$, and their contribution dominates on times $T = O(1/Ro)$ (Newell 1969). A plausible scenario is that three-dimensional near resonances transfer energy toward the two-dimensional plane, and then near-two-dimensional interactions (which are also near-resonant) continue the formation of large-scale cyclonic vortices. We show below that including all near resonances (both three-dimensional and near-two-dimensional near resonances) leads to more efficient energy transfer to large scales and stronger symmetry breaking than only near-two-dimensional near resonances. When near resonances are important (e.g. for $Ro \approx 0.1$ as shown below), then low-resolution simulations are restricted to moderately small Rossby numbers so that the number of near resonances captured by the finite grid is sufficient (see also Pushkarev & Zakharov 2000; Connaughton, Nazarenko & Pushkarev 2001). Although the latter statement begs to be quantified, such a study is beyond the scope of the present paper.

Now we present the results for reduced models of near-resonant triad interactions $\mathscr{I}_R(\epsilon; Ro)$ with $\epsilon = O(1)$ at small but finite $Ro = 0.086$, with $\mathscr{I}_R$ defined in § 3.2. We ask how well the reduced dynamics of resonant triad interactions can approximate the original dynamics including all triad interactions. Figure 7 shows the evolution of energy in the large scales $0 \leqslant k \leqslant 5$ for the full simulation (solid), compared to the reduced models with $\epsilon = 0.3$ (circles) and $\epsilon = 1.0$ (crosses). The modified nonlinear terms are now $NL(\mathscr{I}_R(\epsilon; Ro))$ for $\epsilon = 0.3$ and $\epsilon = 1.0$, and all other parameters are same as for the full simulation. In terms of numbers of triad interactions, $\mathscr{I}_R(\epsilon = 0.3; Ro = 0.086)$ contains about 3.5% of all triad interactions in $\mathscr{I}_F$, and $\mathscr{I}_R(\epsilon = 1.0; Ro = 0.086)$ contains about 12% of all triad interactions in $\mathscr{I}_F$. The dashed line is the large-scale energy evolution for the reduced model with nonlinear term $NL(\mathscr{I}_{2D})$, keeping only two-dimensional interactions, and thus reflects the purely

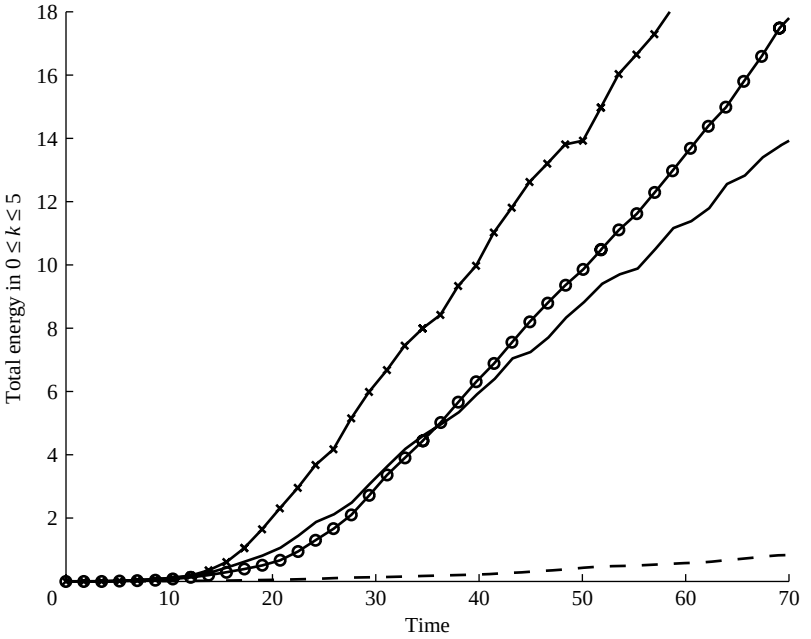

FIGURE 7. Evolution of energy in the large scales $0 \leqslant k \leqslant 5$ for the full simulation (solid), the reduced models including near resonances with $\epsilon = 0.3$ (circles) and $\epsilon = 1.0$ (crosses), and the reduced model including only two-dimensional interactions (dashed).

two-dimensional inverse cascade. The purely two-dimensional interactions $\mathscr{I}_{2D}$ are about 0.6% of all triad interactions. Note that the near resonances $\mathscr{I}_R(\epsilon; Ro)$ contain $\mathscr{I}_{2D}$ (since two-dimensional interactions are exactly resonant), and also include other three-dimensional triad interactions between two-dimensional modes with $k_z = 0$ and three-dimensional modes with $k_z \neq 0$. In figure 7, one sees the dramatically increased energy transfer to large scales for the full simulation compared to the two-dimensional inverse cascade. One also sees that the reduced models including only near resonances for $\epsilon = 0.3$ and $\epsilon = 1.0$ transfer energy to large scales more efficiently than the full simulation including all triad interactions. Thus non-resonances act to reduce energy transfer to large scales. The energy transfer to large scales for near-resonant interactions ($\mathscr{I}_R(0.1; 0.086)$) and ($\mathscr{I}_R(0.2; 0.086)$) (not shown) is faster than for the two-dimensional inverse cascade, but slower than for the full simulation. For $0 \leqslant \epsilon \leqslant 1$, the rate of transfer to large scales increases as ϵ increases, but this trend must reverse itself for some $\epsilon > 1$ as non-resonances are progressively included.

Since multiple-scales analysis does not select a particular value of ϵ, the value $\epsilon = 1.0$ seems the natural choice to define near-resonant interactions by (3.13). However, figure 7 shows that for $\epsilon = 0.3$, the rate of energy input into large scales is not dramatically different from the rate for the full simulation. This is remarkable given that only 3.5% of triad interactions are included in $\mathscr{I}_R(0.3, 0.086)$. Therefore it is worth comparing the spectra for the reduced systems of near resonances with $\epsilon = 0.3$ (figure 8) and of non-resonances with $\epsilon = 0.3$ (figure 9) to the full system, in order to make the point that a small number of near resonances leads to the scaling of the long-time large-scale spectra $E(k) \approx E(k_h; k_z = 0)$ close to $E(k_h; k_z = 0) \propto k_h^{-3}$. Figure 8 shows that, for the same time ($t = 69$), the large-scale spectra for near resonances with $\epsilon = 0.3$ are similar to the large-scale spectra for the full simulation (see also figure 4).

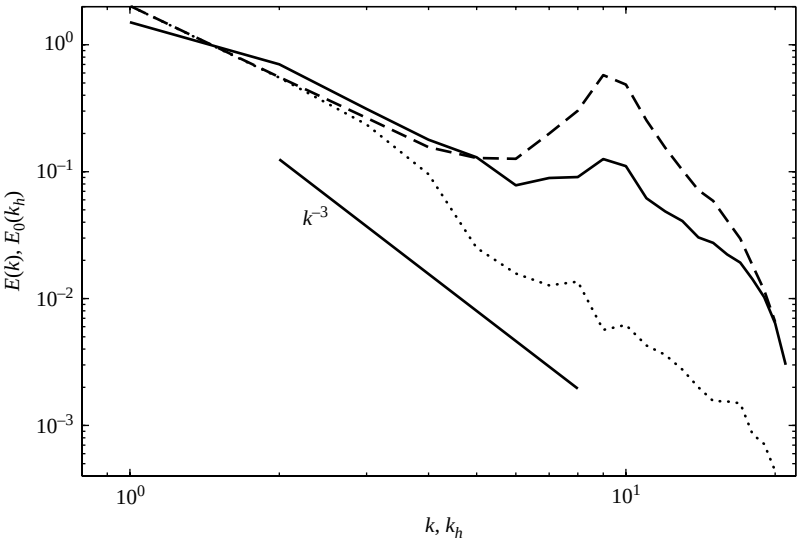

FIGURE 8. $E(k)$ for the full simulation (solid), compared to $E(k)$ (dashed) and $E_0(k_h) = E(k_h; k_z = 0)$ (dotted) for near resonances with $\epsilon = 0.3$. All spectra are at time $t = 69$.

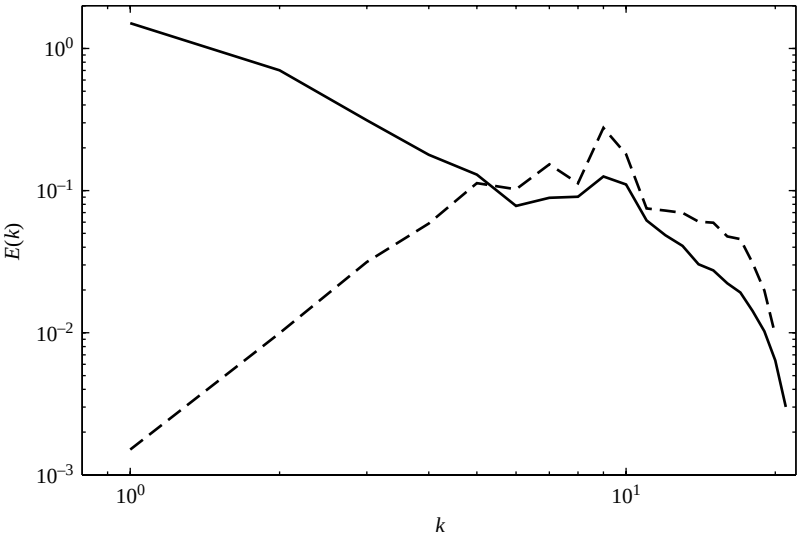

FIGURE 9. $E(k)$ for the full simulation (solid), compared to $E(k)$ for non-resonances with $\epsilon = 0.3$ (dashed). Both are at time $t = 69$.

In sharp contrast, figure 9 shows that there is negligible energy at large scales and long times for the reduced model of non-resonances with $\epsilon = 0.3$, which includes 96.5% of all triad interactions. For the run of figure 9, the nonlinear term in (3.8) was replaced by $NL(\mathscr{I}_F - \mathscr{I}_R(\epsilon; Ro))$ for $\epsilon = 0.3$ and $Ro = 0.086$ (with all other parameters values the same as for the full simulation). Most of the energy input by the forcing is transferred to smaller scales and dissipated by the hyperviscosity. Clearly, non-resonances alone do not generate two-dimensional large scales. This is not surprising since interactions within the two-dimensional plane are excluded (see § 5.1.2).

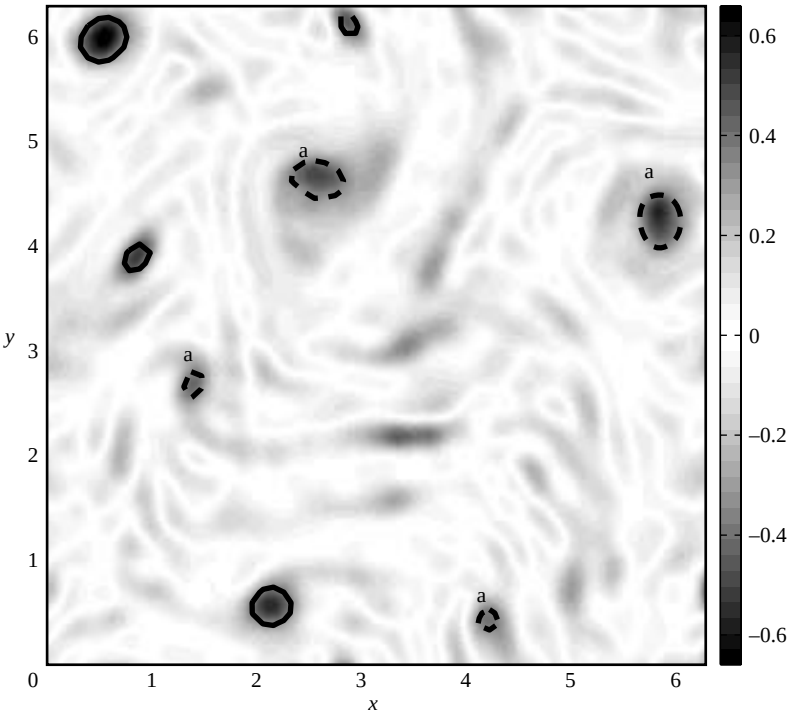

FIGURE 10. Contours of the vertical vorticity of the $\hat{\mathbf{z}}$-averaged velocity at $t = 52$ for the reduced model of near resonances with $\epsilon = 0.3$. Black indicates strong vorticity, and cyclones (anticyclones) are encircled by solid (dashed) contours. Anticyclones are also labelled by the letter a.

In figure 8, notice that there is a higher level of energy near the forced wavenumbers ($k \approx k_f = 10$) compared to the full system or compared to the reduced models including only non-resonances (figure 9). This is because there is only a small number of triads available to pump energy out of the forced modes into other scales. However, this small number of near-resonant triad interactions is apparently enough to extract a portion of the energy from the forced modes to generate two-dimensional large-scale motions. The energy input rates associated with the reduced models of near resonances may be enhanced because of the elevated energy in the forced modes. The large amount of energy near the forcing scale leads to more fine-scale structure than is observed in the full simulation. Since we are interested in the large-scale structure, and since most of the large-scale energy is in two-dimensional two-component modes (u, v) with $k_z = 0$, it is instructive to view the vertical vorticity after filtering three-dimensional motions with $k_z \neq 0$. The vertical vorticity of the $\hat{\mathbf{z}}$-averaged velocity (figure 10) shows large-scale two-dimensional vortices; however, as shown by figure 11, there is now a slight bias toward anticyclones, rather than the strong dominance of cyclones in the full simulation (figures 6 and 14). In figure 11, the time $t = 52$ was chosen for comparison with figure 14. We did not observe cyclone dominance for reduced models of near resonances with values of $\epsilon \leqslant 0.5$. However, the reduced model of near resonances with $\epsilon = 1.0$ shows strong symmetry breaking in favour of cyclones comparable with the full system (see figures 13 and 14).

The value $\epsilon = 1.0$ in (3.13) seems natural to define near-resonant interactions. Next we show that with $\epsilon = 1.0$, the reduced model of near-resonant interactions

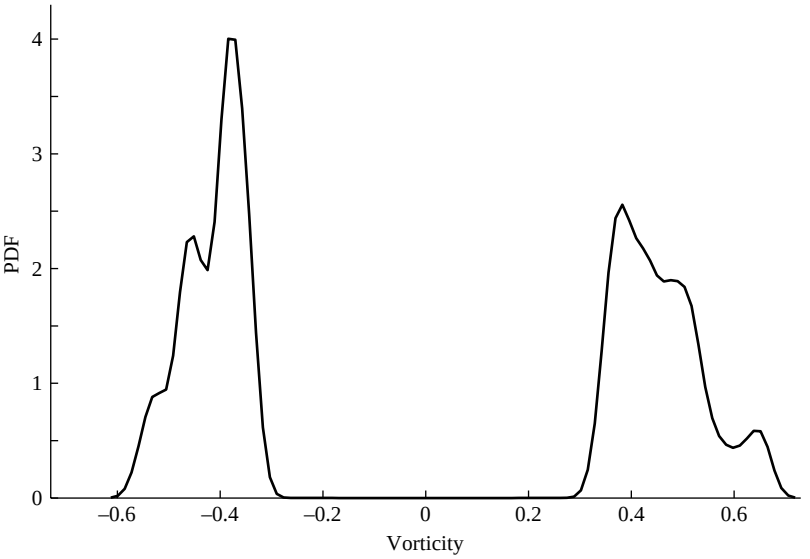

FIGURE 11. PDF of vertical vorticity in the $\hat{\mathbf{z}}$-averaged velocity for the reduced model of near resonances with $\epsilon = 0.3$ at time $t = 52$.

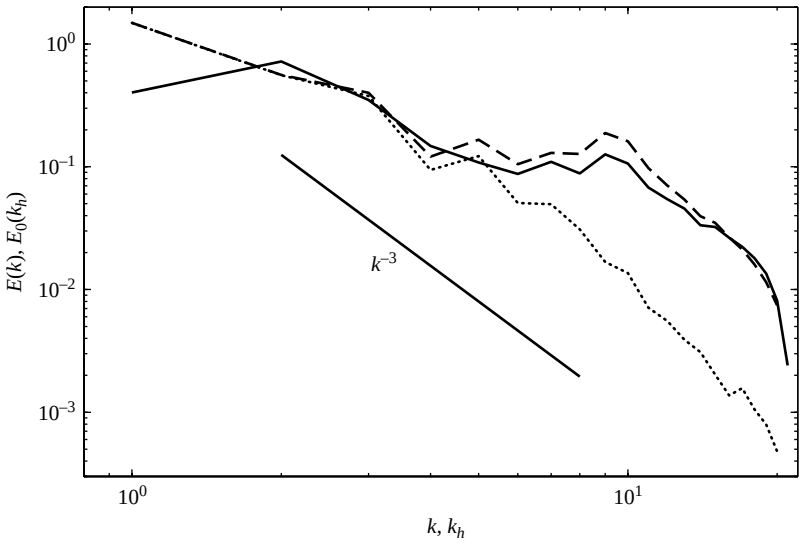

FIGURE 12. $E(k)$ for the full simulation (solid), compared to $E(k)$ (dashed) and $E_0(k_h) = E(k_h; k_z = 0)$ (dotted) for near resonances with $\epsilon = 1.0$. All spectra are at time $t = 52$.

reproduces all distinguishing features of the full simulation at $Ro = 0.086$, including strong cyclone dominance. First, figure 12 compares spectra $E(k)$ and $E(k_h; k_z = 0)$ for near resonances with $\epsilon = 1.0$ to the spectrum $E(k)$ for the full simulation. Since the rate of energy transfer to large scales is faster for near resonances with $\epsilon = 1.0$ than for the full simulation, the time $t = 52$ is chosen for the comparison of spectra. The scaling $E(k) \approx E(k_h; k_z = 0)$ close to $E(k_h; k_z = 0) \propto k_h^{-3}$ is captured by the reduced model. Notice that there is more energy in wavenumbers near the forced wavenumbers compared to the full simulation, but not nearly the excess seen in the reduced model

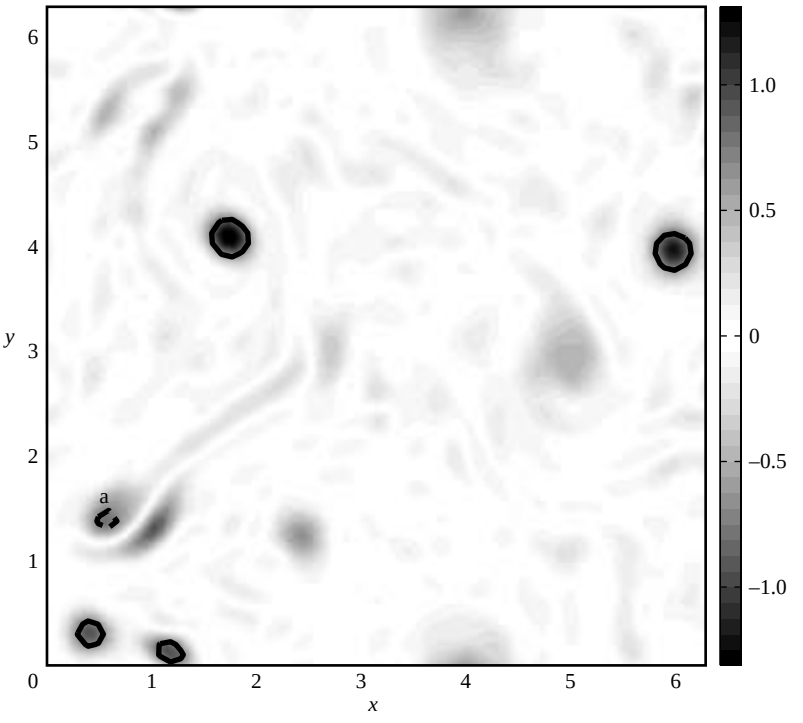

FIGURE 13. Contours of the vertical vorticity of the $\hat{\mathbf{z}}$-averaged velocity at $t = 52$ for the reduced model of near resonances with $\epsilon = 1.0$. Black indicates strong vorticity, and cyclones (anticyclones) are encircled by solid (dashed) contours. Anticyclones are also labelled by the letter a.

of near resonances with $\epsilon = 0.3$ (see figure 8). Contours of the vertical vorticity of the $\hat{\mathbf{z}}$-averaged velocity (figure 13) show clearly the cyclone dominance in the reduced model. A comparison of the PDFs of vertical vorticity (figure 14) shows that the reduced model has even higher values of cyclonic vorticity than the full simulation. Different realizations of the reduced model also showed symmetry breaking in favour of cyclones at least as strong as seen in the full simulation.

5.1.2. *The role of two-dimensional interactions*

With random forcing at small scales, the two-dimensional large scales of three-dimensional rotating turbulence are distinguished from the large scales of two-dimensional non-rotating turbulence by (i) steeper energy spectra, and (ii) the dominance of cyclones over anticyclones. It is well known that two-dimensional turbulence does not exhibit cyclone/anticyclone asymmetry (McWilliams 1984, see also Smith & Yakhot 1994). Thus an inverse cascade in the two-dimensional plane alone does not fully explain the generation of two-dimensional large-scale motions in three-dimensional rotating flows, at least at moderate Rossby numbers where numerical simulations can adequately resolve near resonances. Nevertheless, two-dimensional interactions are crucial for the generation of large scales. Figure 15 shows energy spectra for the dynamics without two-dimensional interactions (nonlinear term $NL(\mathscr{I}_F - \mathscr{I}_{2D})$) and the dynamics of two-dimensional interactions only (nonlinear term $NL(\mathscr{I}_{2D})$). When purely two-dimensional interactions are removed from the full dynamics, the generation of two-dimensional large scales is prevented, indicating the

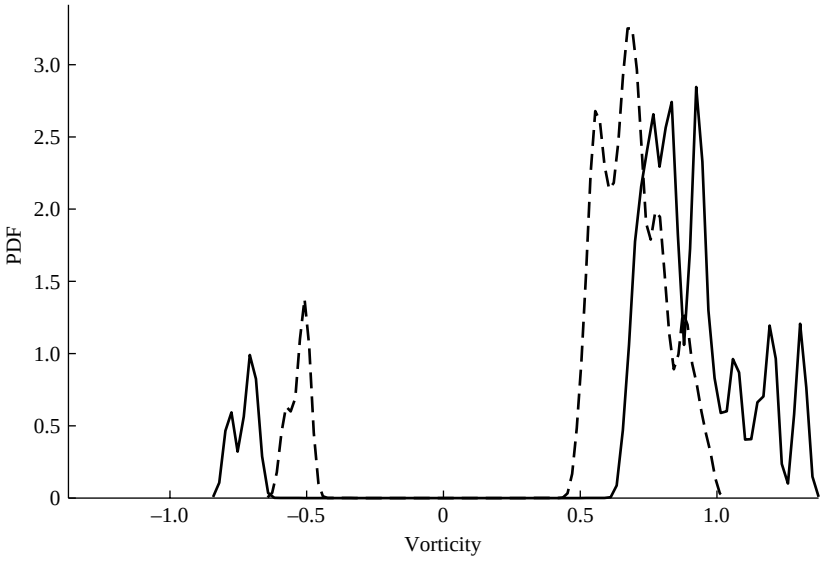

FIGURE 14. PDF of vertical vorticity in the $\hat{\mathbf{z}}$-averaged velocity field at $t = 52$. Near resonances with $\epsilon = 1.0$ (solid) compared to the full simulation (dashed).

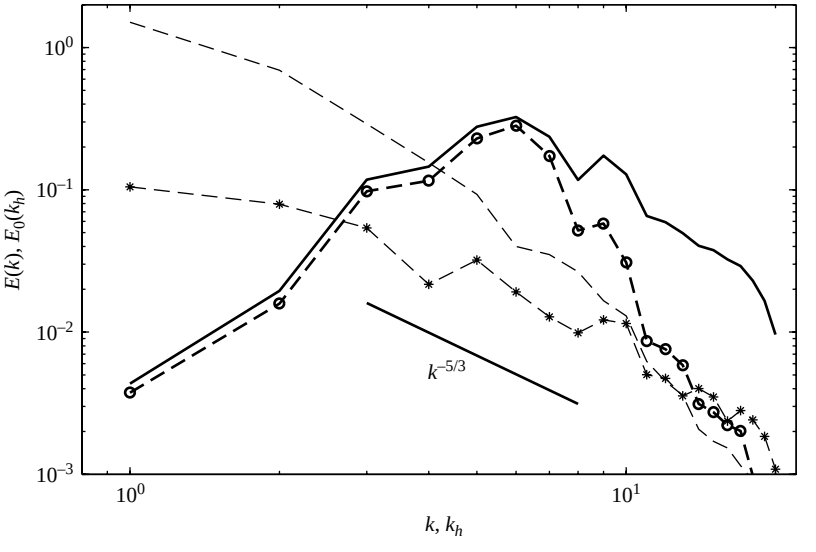

FIGURE 15. $E(k)$ (solid) and $E_0(k_h) = E(k_h; k_z = 0)$ (dashed with circles) for the reduced model with two-dimensional interactions removed ($\mathscr{I}_F - \mathscr{I}_{2D}$). Energy spectrum $E_0(k_h)$ (dashed with stars) for the reduced model with two-dimensional only ($\mathscr{I}_{2D}$). Energy spectrum $E_0(k_h)$ (dashed) for the full simulation. All spectra are at time $t = 69$ except the reduced model of two-dimensional interactions only, which is at $t = 105$.

importance of the inverse cascade in the two-dimensional plane. As already noted, purely two-dimensional interactions $\mathscr{I}_{2D}$ generate large scales with much lower energy compared to the full dynamics, and the energy spectrum scales close to $E_0(k_h) \propto k_h^{-5/3}$. Finally, the PDF of vertical vorticity (figure 16) for the two-dimensional flow at time $t = 105$ indicates symmetry between cyclones and anticyclones, also as expected.

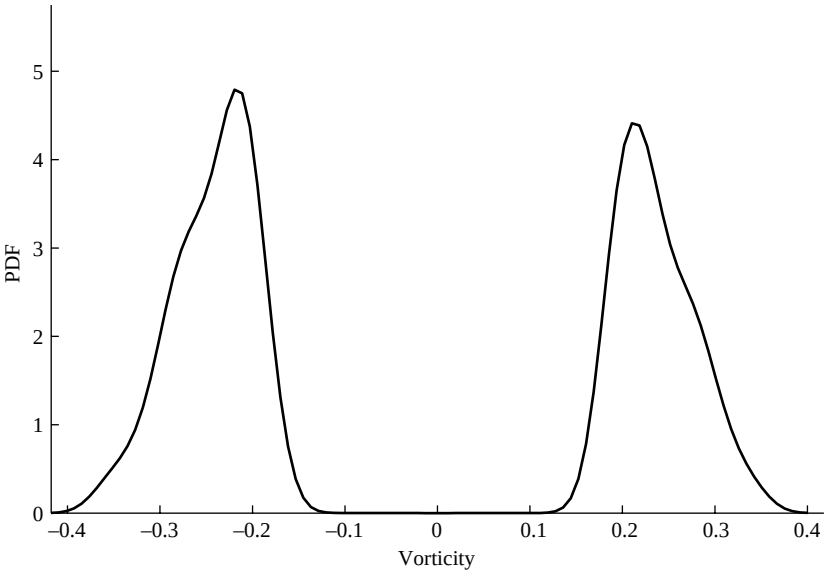

FIGURE 16. PDF of vertical vorticity in the $\hat{\boldsymbol{z}}$-averaged velocity for two-dimensional interactions at time $t = 105$.

θ_w	10°	15°	20°	30°	40°
δ	2.02	3.04	3.98	5.82	7.4873
% interactions	1.98%	4.35%	7.95%	17.56%	26.97%

TABLE 1. The relation between δ, θ_w, and the percentage of near-two-dimensional triad interactions in the wedge defined as (5.3) for $Ro = 0.086$ and resolution 64^3 Fourier modes.

5.1.3. *Near two-dimensional runs*

In this section we compare the dynamics of near-resonant triad interactions to the dynamics of near-two-dimensional triad interactions. The near-resonant interactions defined by (3.13) with $\epsilon = O(1)$ include interactions among three near-two-dimensional modes, all with small $|k_z|$. However, other near-resonant interactions include fundamentally three-dimensional modes with $|k_z|$ large. Here we ask if interactions between near-two-dimensional modes are primarily responsible for the large-scale energy spectra $E(k) \approx E(k_h; k_z = 0) \propto k_h^{-3}$ and the generation of cyclones, or if near-resonant interactions including three-dimensional modes play an important role. To this end, we consider reduced models including only modes with wavenumber in an azimuthal wedge symmetric about the two-dimensional plane,

$$|\sigma_s(\boldsymbol{k})| = \left|\frac{k_z}{k}\right| \leqslant \delta\ Ro \tag{5.3}$$

for a positive δ. This wedge has the half-angle $\theta_w = \sin^{-1}(\delta\ Ro)$ measured from the two-dimensional plane. Table 1 summaries the relations between δ, θ_w, and the percentage of near-two-dimensional triad interactions in each wedge. This reduced dynamics can be simulated by setting to zero, at each time step, the amplitudes of all modes outside the wedge.

Figure 17 compares the time evolution of energy in the large scales with wavenumber $0 \leqslant k \leqslant 5$, for the near-two-dimensional runs with $\theta_w = 15°$ and $\theta_w = 40°$,

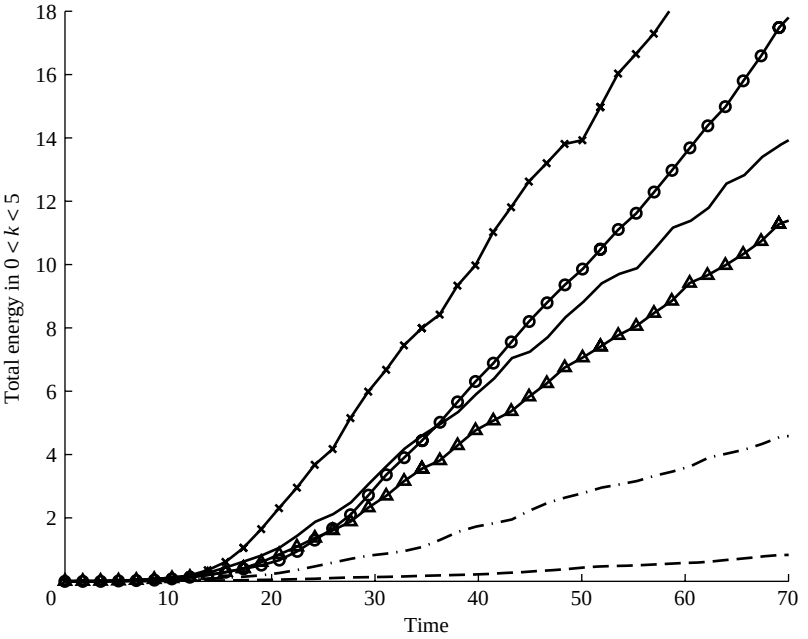

FIGURE 17. Evolution of energy in the large scales $0 \leqslant k \leqslant 5$ for the full simulation (solid), near resonances with $\epsilon = 0.3$ (circles) and $\epsilon = 1.0$ (crosses), near-two-dimensional with $\theta_w = 15^\circ$ (dash-dot) and $\theta_w = 40^\circ$ (triangles), and two-dimensional interactions only (dashed).

the full simulation, the near-resonance runs with $\epsilon = 0.3$ and $\epsilon = 1.0$, and the two-dimensional-only run. Notice that the near-two-dimensional run with $\theta_w = 15^\circ$ has slightly more triad interactions (4.35% of the total number) than the near-resonances run with $\epsilon = 0.3$ (3.5%), but the rate of energy input to large scales for the former (dash-dot) is much slower than that for the latter (circles). This demonstrates that near resonances including three-dimensional interactions are much more efficient than near-two-dimensional interactions alone for the generation of large-scale motions. In fact, the rate of energy input to large scales for the near-two-dimensional runs with $\theta_w \leqslant 40^\circ$ is slower than that of the full simulation, while the rate for near resonances with $0.3 \leqslant \epsilon \leqslant 1.0$ surpasses the rate for the full simulation.

Figure 18 compares spectra for the full simulation to spectra for near-two-dimensional interactions with wedge half-angle of 40°, including about 27% of triad interactions (compare also to figures 8 and 12). At the same time $t = 69$, even for this rather big wedge, the large scales of the near-two-dimensional run have less energy than the large scales of the full simulation. Also interesting is the fact that the near resonances with $\epsilon = 1.0$ (12% of triad interactions) do a much better job of extracting energy from the forced modes than the near-two-dimensional with $\theta_w = 40^\circ$ (27%). This observation is consistent with the emerging picture that three-dimensional near resonances efficiently transfer energy from the three-dimensional forced modes to larger-scale near-two-dimensional modes, and then near-two-dimensional modes (which are also near-resonant) continue the process of large-scale structure formation. Finally, figure 19 shows that symmetry breaking between cyclones and anticyclones is relatively weak for near-two-dimensional interactions in the (large) wedge with half-angle 40° (solid), compared to the full simulation (dashed), and also compared to the run of near resonances with $\epsilon = 1.0$ (figure 14). Thus three-dimensional near

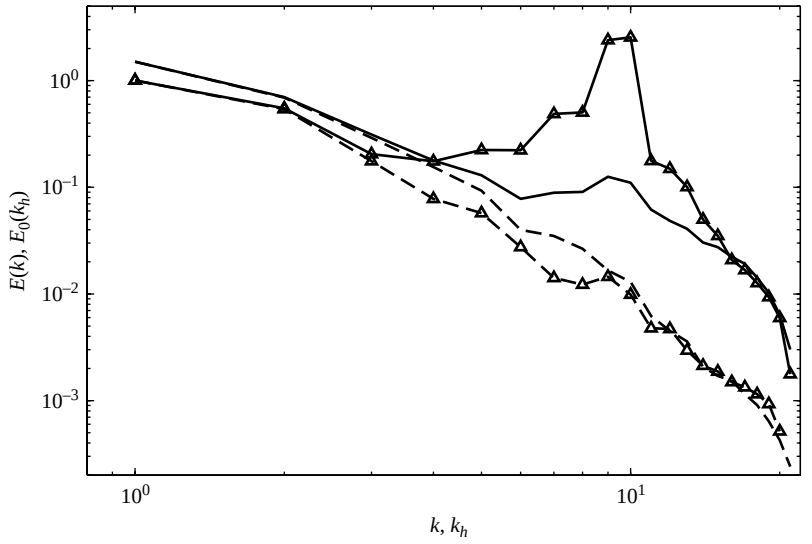

FIGURE 18. $E(k)$ (solid) and $E_0(k_h) = E(k_h; k_z = 0)$ (dashed) for the full simulation, compared to $E(k)$ (solid with symbols) and $E_0(k_h)$ (dashed with symbols) for near-two-dimensional interactions with $\theta_w = 40°$. All spectra are at time $t = 69$.

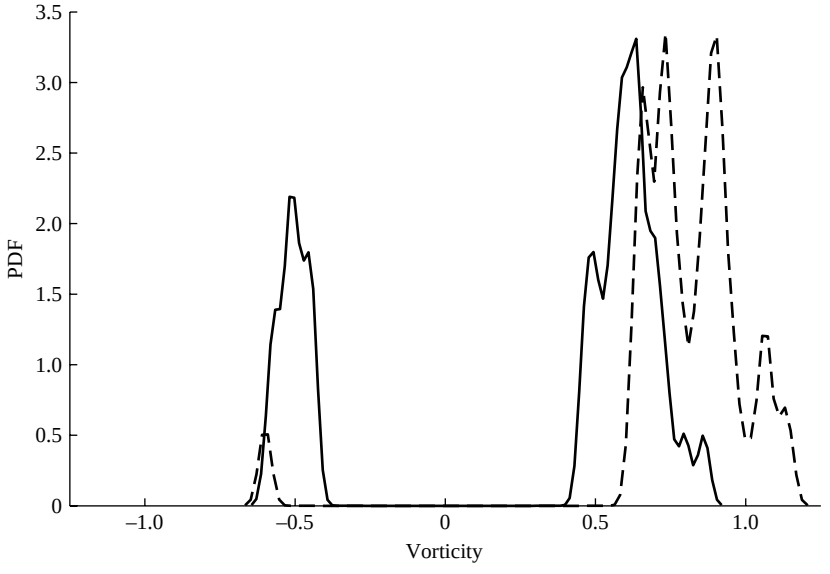

FIGURE 19. PDF of vertical vorticity in the $\hat{\mathbf{z}}$-averaged velocity field at $t = 69$. Near-two-dimensional with $\theta_w = 40°$ (solid) compared to the full simulation (dashed).

resonances appear to be a critical factor in the symmetry breaking and cyclone dominance observed in rotating flows at moderate Rossby number.

6. Summary and discussion

The goal of the study is to identify the mechanisms responsible for the energy transfer to large scale and the formation of large-scale cyclonic vortical columns

in three-dimensional homogeneous rotating turbulence. We perform numerical simulations, using a random force at intermediate scales to inject energy at a constant average rate. Simulations of the full equations of motion are compared to simulation of several reduced models, which include only a subset of all possible triad interactions in Fourier space. When only a subset of triad interactions is retained, then FFTs can no longer be used for efficient calculation of the nonlinear term, and thus all simulations are restricted to 64^3 Fourier modes. The Rossby number for the results shown here is fixed at $Ro = 0.086$, small enough for nonlinear two-dimensionalization in the full system, but large enough that an adequate number of near resonances is captured by the low-resolution grid. Triad interactions in the two-dimensional plane are crucial for generation of two-dimensional large scales, but are not sufficient to explain the scaling of the large-scale energy spectra $E(k) \approx E(k_h; k_z = 0) \propto k_h^{-3}$, nor to explain the formation of coherent vortical columns and the dominance of cyclones. The reduced model of near resonances defined by (3.13) with $\epsilon = 1.0$ captures the large-scale long-time spectral scaling as well as the cyclone dominance. Furthermore, the model of near resonances with $\epsilon = 1.0$, including both three-dimensional and near-two-dimensional near resonances, is more efficient than models including only near-two-dimensional modes with respect to: (i) extraction of energy from three-dimensional forcing at intermediate scales, (ii) efficient generation of two-dimensional large scales, and (iii) strong symmetry breaking in favour of cyclones. Our simulations support the picture that three-dimensional near resonances efficiently transfer energy from three-dimensional modes to larger-scale near-two-dimensional modes, and then near-two-dimensional modes (which are also near-resonant) continue the process of large-scale structure formation (Waleffe 1993; Smith & Waleffe 1999; Majda *et al.* 1999, 2001). Non-resonances, defined here as the complement to near resonances, act largely to extract energy from the forced modes and transfer that energy to smaller scales, where it is dissipated by viscosity. We have performed simulations at two other sets of parameters (i) $k_f = 10$, $\Omega = 38$, $\epsilon_f = 0.7$ ($Ro = 0.054$), (ii) $k_f = 13$, $\Omega = 48$, $\epsilon_f = 0.86$ ($Ro = 0.055$), and all results are consistent with the results shown here for $Ro = 0.086$. Finally, we have simulated the reduced model of near resonances on the β-plane (defined analogously to (3.13) with $\epsilon = 1.0$), and find the generation of zonal flows and scaling of the large-scale spectra $E(k) \approx E(k_y; k_x = 0) \propto k_y^{-5}$ (Lee 2003), as in the full simulation (Chekhlov *et al.* 1996). The results for reduced models of the β-plane will be presented separately.

Our reduced models and the weakly nonlinear analysis for small $|k_z|/k_h$ by Galtier (2003) and Cambon *et al.* (2004) predict that the quasi-two-dimensional state of rotating turbulence at small Ro is different from purely two-dimensional flow. The asymptotic equations for rapidly rotating flow derived by Julien *et al.* (1998) also admit linear waves with frequencies proportional to $\pm k_z/k_h$, thus assuming $|k_z| \ll k_h$. The assumption of small $|k_z|$ restricts the dynamics to an azimuthal wedge symmetric about the two-dimensional plane, as in our reduced models including only near-two-dimensional modes. Our simulations suggest, however, that approximate equations derived for small $|k_z|$ will exhibit weaker symmetry breaking between cyclones and anticyclones than the full equations and the reduced model including all near resonances between fast waves with $|k_z|/k = O(1)$ (and for $\epsilon = 1.0$).

The present work combines aspects of fundamental turbulence research and modelling for geophysical applications. Many fundamental studies of forced three-dimensional turbulence, including rotating and stratified turbulence, focus on the forward transfer of energy to small scales. For dispersive-wave turbulence, we have directed our attention to the slow leakage of energy to scales larger than the forcing

scales (see also Smith & Waleffe 2002). The accumulation of energy in large-scale coherent structures over long time scales may be relevant to long-time modelling of geophysical flows. Our work on three-dimensional rotating and stratified flows suggests that the long-time behaviour of geophysical models depends strongly on faithful representation of the resonant wave interactions. Models which change significantly the dispersion relation of the original system may not accurately capture long-time coherence at large scales.

A case in point is the hydrostatic approximation for $k_h/|k_z| \ll 1$ and $f/N \ll 1$: since the hydrostatic approximation excludes small-scale horizontal motions, it necessarily alters the characteristics of energy leakage from small to large scales. The mechanisms for this leakage may be determined by the resonant traces and thus the dispersion relation. The hydrostatic equations have waves with dispersion relation $\sigma_h(\boldsymbol{k}) = \pm (N^2k_h^2 + f^2k_z^2)^{1/2}/|k_z|$, compared to the Boussinesq equations with dispersion relation $\sigma_b(\boldsymbol{k}) = \pm (N^2k_h^2 + f^2k_z^2)^{1/2}/k$. While the latter equations have linear wave frequencies between the values N and f, the former equations admit diverging linear wave frequencies when $k_z/k_h \to 0$, and the resonant traces are highly distorted. One can argue that modes with $|k_z|$ small should not be considered within the hydrostatic approximation, but they are present in numerical simulations and in physical flows. The impact of near-resonant wave interactions for long-time geophysical modelling of rotating and stratified flows will be the subject of future research.

Both authors gratefully acknowledge support from the National Science Foundation under grants NSF-DMS-0071937 (L.M.S. and Y.L.) and NSF-DMS-0305479 (L.M.S). F. Waleffe has given valuable input to both authors during the duration of this work. L.M.S. thanks C. Cambon, P. A. Davidson and R. Rubinstein for many stimulating discussions and helpful comments/suggestions.

REFERENCES

Babin, A., Mahalov, A. & Nicolaenko, B. 1996 Global splitting, integrability and regularity of 3d euler and navier stokes equations for uniformly rotating fluids. *Eur. J. Mech.* B/*Fluids* **15**, 291–300.

Babin, A., Mahalov, A. & Nicolaenko, B. 2000 Fast singular oscillating limits and global regularity for the 3d primitive equations of geophysics. *Math. Modell. Numer. Analysis* **34**, 201–222.

Bardina, J., Ferziger, J. & Rogallo, R. 1985 Effect of rotation on isotropic turbulence: Computation and modeling. *J. Fluid Mech.* **154**, 321–336.

Baroud, C., Plapp, B., Swinney, H. & She, Z. 2003 Scaling in three-dimensional and quasi two-dimensional rotating turbulent flows. *Phys. Fluids* **15**, 2091–2104.

Bartello, P. 1995 Geostrophic adjustment and inverse cascades in rotating stratified turbulence. *J. Atmos. Sci.* **52**, 4410–4428.

Bartello, P., Metais, O. & Lesieur, M. 1994 Coherent structures in rotating three-dimensional turbulence. *J. Fluid Mech.* **273**, 1–29.

Bellet, F., Godeferd, F., Scott, J. & Cambon, C. 2004 Wave-turbulence in rapidly rotating flows. *J. Fluid Mech.* (submitted).

Benney, D. & Saffman, P. 1966 Nonlinear interaction of random wave in a dispersive medium. *Proc. Roy. Soc. London Ser.* A **289**, 301–320.

Boyd, J. 2001 *Chebyshev and Fourier Spectral Methods*, 2nd edn. Dover.

Cambon, C. & Jacquin, L. 1989 Spectral approach to non-isotropic turbulence subjected to rotation. *J. Fluid Mech.* **202**, 295–317.

Cambon, C., Mansour, N. & Godeferd, F. 1997 Energy transfer in rotating turbulence. *J. Fluid Mech.* **337**, 303–332.

Cambon, C., Mansour, N. & Squires, K. 1994 Anisotropic structure of homogeneous turbulence subjected to uniform rotation. *Center for Turb. Res., Stanford, Proc. of the Summer Program.*

Cambon, C., Rubinstein, R. & Godeferd, F. 2004 Advances in wave turbulence: rapidly rotating flows. *New J. Phys.* **6**, 73.

Canuto, C., Hussaini, M., Quarteroni, A. & Zang, T. 1988 *Spectral Methods in Fluid Dynamics*. Springer.

Canuto, V. & Dubovikov, M. 1997 Physical regimes and dimensional structure of rotating turbulence. *Phys. Rev. Lett.* **78**, 666–669.

Chekhlov, A., Orszag, S., Galperin, B., Sukoriansky, S. & Staroselsky, I. 1996 The effect of small-scale forcing on large-scale structures in two-dimensional flows. *Physica* D **98**, 321–334.

Chen, Q., Chen, S., Eyink, G. & Holm, D. 2004 Resonant interactions in rotating homogeneous three-dimensional turbulence. *J. Fluid Mech.* (submitted).

Connaughton, C., Nazarenko, S. & Pushkarev, A. 2001 Discreteness and quasiresonances in weak turbulence of capillary waves. *Phys. Rev.* E **63**, 046306.

Constantin, P. 2004 Transport in rotating fluids. *Discrete Continuous Dyn. Syst.* **10**, 165–176.

Constantin, P. & Majda, A. 1988 The beltrami spectrum fo incompressible fluid flows. *Commun. Math. Phys.* **115**, 435–456.

Embid, P. & Majda, A. 1996 Averaging over fast gravity waves for geophysical flows with arbitrary potential vorticity. *Commun. Partial Diff Equat.* **21**, 619–658.

Embid, P. & Majda, A. 1998 Low froude number limiting dynamics for stably stratified flow with small or finite rossby numbers. *Geophys. Astrophys. Fluid Dyn.* **87**, 1–50.

Galtier, S. 2003 Weak inertial-wave turbulence theory. *Phys. Rev.* E **68**, 015301.

Greenspan, H. 1969 On the nonlinear interaction of inertial modes. *J. Fluid. Mech.* **36**, 257–264.

Greenspan, H. 1990 *The Theory of Rotating Fluids* (revised edn.) Breukenlen.

Hakim, G., Snyder, C. & Muraki, D. 2002 A new surface model for cyclone-anticyclone asymmetry. *J. Atmos. Sci.* **59**, 2405–2420.

Hopfinger, E., Browand, K. & Gagne, Y. 1982 Turbulence and waves in a rotating tank. *J. Fluid Mech.* **125**, 505–534.

Hossain, M. 1994 Reduction in the dimensionality of turbulence due to a strong rotation. *Phys. Fluids* **6**, 1077–1080.

Huang, H., Galperin, B. & Sukoriansky, S. 2001 Anisotropic spectra in two-dimensional turbulence on the surface of a rotating sphere. *Phys. Fluids* **13**, 225–240.

Jacquin, L., Leuchter, O., Cambon, C. & Mathieu, J. 1990 Homogeneous turbulence in the presence of rotation. *J. Fluid Mech.* **220**, 1–52.

Janssen, P. 2002 Nonlinear four-wave interactions and freak waves. *J. Phys. Oceanogr.* **33**, 863–884.

Jeong, J. & Hussain, F. 1995 On the identification of a vortex. *J. Fluid Mech.* **285**, 69–94.

Julien, K., Knobloch, E. & Werne, J. 1998 A new class of equations for rotationally constrained flows. *Theoret. Comput. Fluid Dyn.* **11**, 251–261.

Kraichnan, R. 1967 Inertial-range in two-dimensional turbulence. *Phy. Fluids* A **10**, 1417–1423.

Lee, Y. 2003 Anisotropic energy transfer in beta-plane and rotating flows. Ph.D thesis, Univ. of Wisconsin, Madison.

Lelong, P. & Riley, J. 1991 Internal wave-vortical mode interactions in strongly stratified flows. *J. Fluid Mech.* **232**, 1–19.

Lollini, L. & Godeferd, F. 1999 Direct numerical simulations of turbulence with confinement and rotation. *J. Fluid Mech.* **393**, 257–307.

Longhetto, A., Montabone, L., Provenzale, A., Didelle, H., Giraud, C., Bertoni, D. & Forza, R. 2002 Coherent vortices in rotating flows: a laboratory view. *Il Nuovo Cimento* **25**, 233–249.

Longuet-Higgins, M. & Gill, A. 1967 Resonant interactions between planetary waves. *Proc. R. Soc. Lond.* A **299**, 120–140.

Majda, A. & Embid, P. 1998 Averaging over fast gravity waves for geophysical flows with unbalanced initial data. *Theoret. Comput. Fluid Dyn.* **11**, 155–169.

Majda, A., Timofeyev, I. & Vanden-Eijnden, E. 1999 Models for stochastic climate prediction. *Proc. Natl. Acad. Sci. USA* **96**, 14687–14691.

Majda, A., Timofeyev, I. & Vanden-Eijnden, E. 2001 A mathematical framework for stochastic climate models. *Commun. Pure Appl. Maths* **LIV**, 891–974.

Manfroi, A. & Young, W. 2002 Stability of β-plane kolmogorov flow. *Physica* D **162**, 208–232.

Marcus, P., Kundu, T. & Lee, C. 2000 Vortex dynamics and zonal flows. *Phys. Plasmas* **7**, 1630–1640.

McWilliams, J. 1984 The emergence of isolated coherent vortices in turbulent flow. *J. Fluid Mech.* **146**, 21–43.

McWilliams, J. 1990 The vortices of geostrophic turbulence. *J. Fluid Mech.* **219**, 387–404.

McWilliams, J., Weiss, J. & Yavneh, I. 1999 The vortices of homogeneous geostrophic turbulence. *J. Fluid Mech.* **401**, 1–26.

Morinishi, Y., Nakabayashi, K. & Ren, S. 2001 Dynamics of anisotropy on decaying homogeneous turbulence subjected to system rotation. *Phys. Fluids* **13**, 2912–2922.

Muraki, D., Snyder, C. & Rotunno, R. 1999 The next-order corrections to quasigeostrophic theory. *J. Atmos. Sci.* **56**, 1547–1560.

Newell, A. 1969 Rossby wave packet interactions. *J. Fluid Mech.* **35**, 255–271.

Pedlosky, J. 1986 *Geophysical Fluid Dynamics*. Springer.

Phillips, O. 1968 The interaction trapping of internal gravity waves. *J. Fluid Mech.* **34**, 407–416.

Polvani, L., McWilliams, J., Spall, M. & Ford, R. 1994 The coherent structures of shallow-water turbulence: Deformation radius effects, cyclone/anticyclone asymmetry and gravity-wave generation. *Chaos* **4**, 177–186.

Pushkarev, A. & Zakharov, V. 2000 Turbulence of capillary waves - theory and numerical simulation. *Physica* D **135**, 98–116.

Salmon, R. 1998 *Lectures on Geophysical Fluid Dynamics*. Oxford University Press.

Smith, K. S. 2004 A local model for planetary atmospheres forced by small-scale convection. *J. Atmos. Sci.* **61**, 1420–1433.

Smith, L. & Waleffe, F. 1999 Transfer of energy to two-dimensional large scales in forced, rotating three-dimensional turbulence. *Phys. Fluids* **11**, 1608–1622.

Smith, L. & Waleffe, F. 2002 Generation of slow, large scales in forced rotating, stratified turbulence. *J. Fluid Mech.* **451**, 145–168.

Smith, L. & Yakhot, V. 1994 Finite-size effects in forced two-dimensional turbulence. *J. Fluid Mech.* **274**, 115–138.

Waleffe, F. 1992 The nature of triad interactions in homogeneous turbulence. *Phys. Fluids* A **4**, 350–363.

Waleffe, F. 1993 Inertial transfers in the helical decomposition. *Phys. Fluids* A **5**, 677–685.

Wigeland, R. & Nagib, H. 1978 Grid-generated turbulence with and without rotation about the streamwise direction. *Illinois Institute of Technology Fluids and Heat Transfer Rep.* R78-1.

Zakharov, V., Lvov, V. & Falkovich, G. 1992 *Wave Turbulence*. Springer.